UNIVERZITET U NOVOM SADU
PRIRODNO-MATEMATIČKI
FAKULTET
DEPARTMAN ZA FIZIKU

Kvantitativna radiografija helijumskim snopom sa primenom na antropomorfni karlični fantom

- master rad -

Mentor:
Prof. dr Jovana Nikolov

Kandidat:
Sonja Surla

Novi Sad, januar 2020. god.

Napomena:

Ovaj rad je nastao tokom programa razmene studenata u Hajdelbergu, u Nemačkom centru za istraživanje raka (Deutsches Krebsforschungszentrum). Stoga, rad je uz odobrenje veća deparmana za fiziku Prirodno-matematičkog fakulteta Univerziteta u Novom Sadu napisan na engleskom jeziku uz priloženi sažetak na srpskom jeziku.

Zahvaljujem svom istraživačkom timu na čelu sa dr Mária Martisíková, iz Nemačkog centra za istraživanje raka (Deutsches Krebsforschungszentrum) u Hajdelbergu, gde je nastao ovaj rad. Posebno se zahvaljujem dr Tim Gehrke na korisnim sugestijama tokom pisanja rada.

Veliku i iskrenu zahvalnost dugujem mentorki dr Jovani Nikolov na pruženoj prilici, poverenju i posvećenosti tokom izrade rada.

Hvala roditeljima za razumevanje i nesebičnu ljubav
Vesni, za zrele savete mlađe sestre
Prijateljima, za uspomene
Nikoli, za strpljenje i podršku.

Sažetak

Uvod

Radioterapija je jedna od metoda lečenja malignih tumora. Često se koristi u kombinaciji sa ostalim metodama kao što su hemoterapija i hiruški zahvati. Radioterapija koristi jonizujuće zračenje za uništavanje malignih ćelija. Osnovni cilj radioterapije je da isporuči dovoljnu dozu zračenja u okviru tumora, a što je moguće manje izvan njega. U praksi je nemoguće potpuno zaštititi zdravo tkivo od zračenja, ali se intenzivno radi na smanjenju doze izvan tumora kako bi se umanjili neželjeni efekti radijacione terapije.

Tadicionalna radioterapija rendgenskim zracima često oštećuje zdravo tkivo koje se nalazi u blizini tumora, naročito na putu zračenja do dubine na kojoj se nalazi tumor. Sa druge strane, radioterapijom akceleratorski ubrzanim jonima, kao što su npr. joni vodonika, helijuma ili ugljenika, veoma precizno može da se zračenje fokusira u okviru tumora i na taj način da se zaštite okolna tkiva od neželjenog zračenja. Terapija ubrzanim jonima je prvi put predložena od strane Roberta Wilsona 1946. god. a prva kllinička primena protonskog snopa u radioterapiji je izvršena 1954. god. u Berkliju, Kalifornija. Danas, interesovanje za radioterapiju ubrzanim jonima raste velikom brzinom. Širom sveta u funkciji je više od 75 postrojenja za radioterapiju ubrzanim jonima, a još oko 40 postrojenja su pod rekonstrukcijom sa planiranim početkom rada pre 2021. god. Do kraja 2018. godine 221528 pacijenata su zračeni snopom ubrzanih jona u cilju lečenja malignih obolenja. Pokazalo se takođe, da je terapija ubrzanim jonima dala bolje rezultate od konvencionalne terapije fotonima.

Joni prolazeći kroz materijalnu sredinu najveći iznos energije gube pri kraju svog dometa. Kriva doze zračenja koju ubrzani joni proizvode na svom putu na završnom delu ima vidljivi uspon, a zatim nagli pad (slika 1). Taj deo krive se naziva Braggov pik i cilj je da se on usmeri u zapreminu tumora kako bi se tu oslobodila najveća doza zračenja. Braggov pik je moguće postavljati na potrebnu dubinu menjanjem energije jonskog snopa.

Pored prednosti koju pruža radioterapija ubrzanim jonima, oslobađanje velike doze zračenja na koncentrisanom mestu na putu zračenja, ipak ona može biti i veliki rizik ako se Braggov pik ne pozicionira precizno u tumor. Postupak preciznog pozicioniranja Braggovog pika u tumor je najveći izazov ovog tipa radioterapije. Savremene dijagnostičke metode mogu vrlo precizno da oslikaju tumor i njegov položaj u telu pacijenta. Danas se najčešće koristi kompjuterska tomografija (CT) rendgenskim zracima u vidu CT simulatora za planiranje radioterapijske procedure. Da bi se odredila adekvatna energija jona koji se koriste za zračenje, potrebno je znati njihov domet u heterogenom telu pacijenta. Zato se koristi pretvaranje vrednosti atenuacije rendgenskih zraka od strane različitih vrsta tkiva u relativnu zaustavnu moć sredine kroz koju prolazi snop ubrzanih jona. Pri ovoj konverziji se pravi neizbežna greška od oko 3%. Da bi se izbegla ova nesigurnost u određivanju dometa jona u telu pacijenta, došlo se na ideju da se se pre radioterapije sa ubrzanim jonima izvrši radiografija sa ubrzanim jonima kao dodatak CT simulatoru. Radiografija ubrzanim jonima koristi isti tip zračenja kao i radioterapija ubrzanim jonima, pa se stoga izostavlja nepoželjna nesigurnost konverzije.

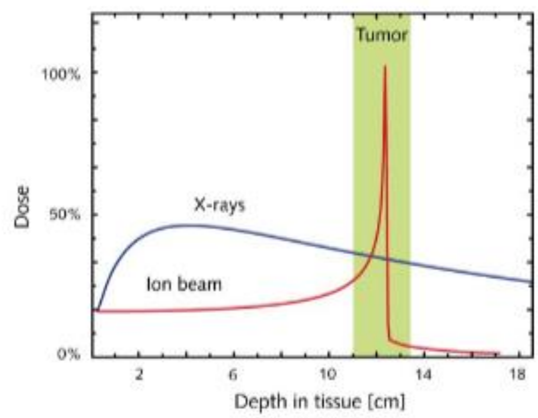

Slika 1: Poređenje doze zračenja kao funkcije dubine u tkivu za X-zrake (konvencionalna radioterapija) i jonski snop (terapija ubrzanim jonima).

Za radiografiju sa ubrzanim jonima, koriste se veće energije nego za terapiju. Braggov pik se postavlja na detektor iza pacijenta. Pri tome se isporucuje samo veoma mala doza zračenja pacijentu, dok se iza pacijenta meri deponovana energija jona u tankom sloju detektora. Sa ovom zabeleženom informacijom za svaki pojedinačni jon iz snopa može se dobiti informacija o integralnoj zaustavnoj moći sredine kroz koju prolaze joni. Što nam dalje pruža mogućnost da lako odredimo energiju jona za terapiju kako bi se Braggov pik tačno našao u okviru tumora. Da bi se integralna zaustavna moć medijuma heterogenog tkiva pacijenta izrazila u opštim jedinicama, uvodi se pojam – „debljina ekvivalenta vode“ (*WET, Water Equivalent Thickness*), odnosi se na debljinu vodenog fantoma koji ima istu zaustavnu moć kao određeni medijum kroz koji zračenje prolazi. Najveća prednost radiografije ubrzanim jonima je ta što se može izvršiti neposredno pred terapiju ubrzanim jonima sa istom postavkom pacijenta. Poređenjem radiografskog snimka dobijenog jonima sa radiografskim snimkom dobijenog rengenskim zracima mogu se videti potencijalne razlike u „debljini ekvivalenta vode“ što može biti posledica pomerene geometrije pozicioniranja pacijenta ili promene u telu pacijenta (npr. gubitak težine ili proširenje tumora). Ideja je da se uporede WET mape dobijene CT simulatorom i metodom radiografije ubrzanim jonima. Razlike u WET vrednostima dobijenih sa ove dve metode bi značile pogrešnu postavku pacijenta za radioterapiju ili anatomske promene u telu pacijenta.

Materijal i metode

Svi eksperimenti u ovoj tezi su rađeni u Centru za terapiju ubrzanim jonima u Hajdelbergu (Heidelberg Ion-Beam Therapy Center, HIT), u Nemačkoj. Ovaj centar je prvo postrojenje za radioterapiju ubrzanim jonima vodonika i ugljenika u Evropi, osnovan 2009. god. Sadrži tri sobe za terapiju i jednu sobu za eksperimentalna istraživanja. Dve sobe opremljene su horizontalnim fiksiranim snopom za lečenje pacijenta, a jedna sa 360° rotirajućim nosačem (gantrijem), tako da se snop jona može usmeravati ka pacijentu iz proizvoljnih smerova. Pored jona protona (^{1}H) i ugljenika (^{12}C), koji se koriste u kliničkoj praksi, dostupni su još i joni helijuma (^{4}He) i kiseonika (^{16}O). Svi eksperimenti predstavljeni u ovom radu izvedeni su u eksperimentalnoj sobi sa fiksnim horizontalnim snopom.

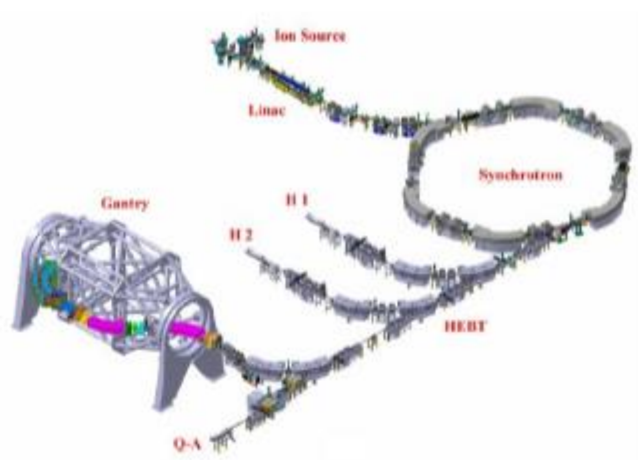

Slika 2: Pregled akceleratora u HIT objektu. Prikazane su dve sobe za pacijente sa horizontalno fiksisanim snopovima (H1, H2), jedna soba sa 360◦ rotirajućim nosačem (Gantri) i eksperimentalna soba (Q-A).

Protoni se proizvode od vodoničnog gasa, dok se za proizvodnju ugljenokovih jona koristi ugljen-dioksid. Jednom kada se proizvodu joni od interesa oni se najpre ubrzavaju u linearnom akceleratoru. Ovde se joni ubrzavaju do 10% brzine svetlosti. Tako ubrzani joni se ubrizgavaju u sinhrotron gde se mogu ubrzati do 255 diskretnih energija, što odgovara rasponu od 20 mm do

300 mm dometa u vodi. Prednost upotrebe sinhrotrona je što može ubrzati jonski snop do različitih energija. Nakon izlaska snopa iz sinhrotrona, joni se usmeravaju u prostorije za terapiju preko sistema za transport visokoenergetskih snopova. Dipolni magneti služe sa skretanje, dok se kvadrupolni magneti koriste za fokusiranje snopa.

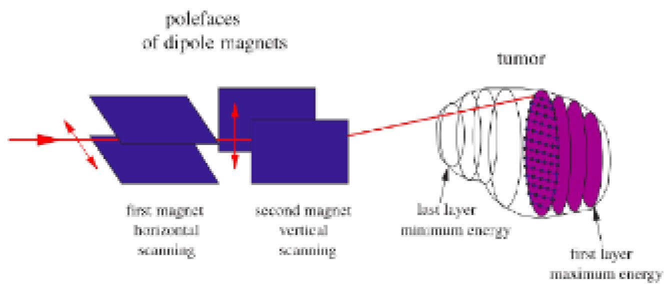

Slika 3: Magneti za skretanje i fokusiranje snopa jona.

Detektori korišćeni za snimanje radiografa sa ubrzanim jonima su TimePix detektori, konstruisani u CERN-u. Osetljivi sloj detektora je 14 mm x 14 mm, podeljeno na 256 x 256 piksela, sa veličinom od 55 µm x 55 µm. Ovaj osetljivi sloj napravljen je od kristalnog silicijuma debljine 300 µm i svaki piksel je posebno vezan je za čip za očitavanje. TimePix je poluvodički detektor n-tipa sa koncentracijom donora od približno (0,34 ± 0,09) x10^{12} cm^{-3}. Svaki piksel ima svoju elektroniku i posebno napajanje, što omogućava nezavisna podešavanja i rad svakog piksela posebno.

Slika 4: Timepix detector (1), matična ploča (2), napajanje (3), interfejs za očitavanje (4).

Detektor je priključen na matičnu ploču koja povezuje detektor i interfejs za očitavanje (slika 4). Više detektora se može učvrstiti na istu matičnu ploču. Kada se priključe na istu matičnu ploču, one se automatski sinhronizuju. Interfejs za očitavanje je povezan sa računarom preko USB kabla, gde parametre detektora kontroliše programski paket *Pixet*. Pomoću ovog softvera moguće je podesiti režim rada, prag signala, dužinu rama, takt frekvenciju, napon i mnoge druge postavke. Interfejs za očitavanje podataka prikuplja podatke u ramovima. Ram je vreme prikupljanja podataka (aktivno vreme). Između dva okvira je odgovarajući vremenski interval, tokom koga se podaci ne prikupljaju, već obrađuju pre početka sledećeg rama (mrtvo vreme). Interfejs omogućava snimanje do 90 ramova u sekundi sa jednim detektorom.

Svaki piksel detektora može da radi u jednom od četiri režima rada detektora:

1. Brojač (counting mode) služi za merenje broja jona koji prolaze kroz detektor
2. Merenje energije pojedinačnih jona (energy mode)
3. Merenje vremena udara jona na detektor (time mode)
4. Maskirani režim (masked mode) - za deaktivaciju oštećenih piksela

U ovoj tezi pet detektora je radilo u režimu merenja vremena udara jona na detector, a jedan u režimu merenja energije jona.

Za snimanje radiografa sa ubrzanim jonima korišćena su šest TimePix detektora. Ovi detektori su postavljeni paralelno, dva ispred i četiri detektora iza pacijenta/fantoma. Prva dva detektora su u paru postavljena ispred pacijenta (prednji sistem za praćenje putanje jona), druga dva detektora su takođe postavljena u paru iza pacijenta (zadnji sistem za praćenje putanje jona) i oni služe za praćenje pojedinačnih jona tokom njihove putanje. Sva ova četiri detektora rade u režimu merenja vremena udara jona u detektor. Ovo omogućava praćenje pojedinačnih jona i rekonstrukciju njihovih putanja što je bitno za konstruisanje radiografske slike. Pretposlednji detektor u nizu koji je postavljen iza pacijenta služi za merenje energije jona. Poslednji detektor u nizu koji je u paru sa detektorom za merenje energije radi u režimu merenja vremena i omogućava dodatnu informaciju kada joni udaraju u poslednji par detektora, s obzirom da ova informacija nedostaje detektoru koji radi u režimu merenja energije.

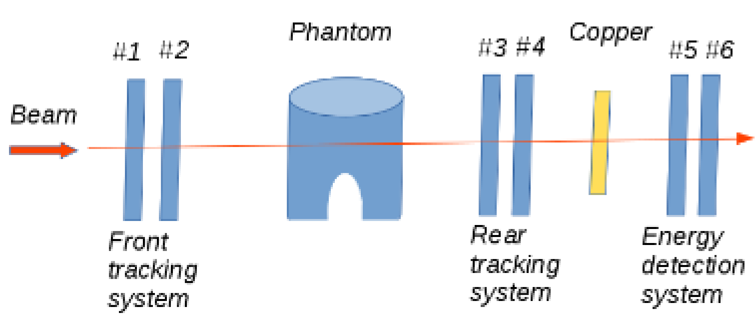

Slika 5: Šematski prikaz eksperimentalne postavke

Između zadnjeg sistema za praćenje jona i sistema za detekciju energije jona se nalazi bakarni kolimator koji apsorbuje energiju jona kako bi se rastući deo Braggovog pika našao na detektoru #5. Više energije jona su poželjnije za snimanje radiografa jer joni s većim energijama trpe manje skretanja uzrokovanog Kulonovim silama i omogućavaju bolju rekonstrukciju putanje, što stvara bolju prostornu rezoluciju konačne slike. Takođe, veće energije smanjuju apsorbovanu dozu u fantomu/pacijentu. Rastući deo Braggovog pika se postavlja na detektor za merenje energije jona kako bi i za male razlike u WET izmerio veliku razliku u deponovanoj energiji jona u detektoru.

Debljina ekvivalenta vode izmerena helijumskim snopom odgovara debljini ekvivalenta vode izmerenoj protonskim i ugljeničnim snopovima. Helijumski jonski snop je odabran u eksperimentima jer trpi manje Kulonovog rasejanja od protonskog snopa i manje fragmentacije od ugljeničnog.

Za pretvaranje izmerene deponovane energije jona u debljinu ekvivalenta vode korišćene su kalibracione krive (slika 6) dobijene u prethodnom istraživanju u okviru iste istraživačke grupe. Za različite debljine istog materijala merena je deponovana energija jona u detektoru iza njega. Tako je merena deponovana energija jona u detektoru iza materijala poznate debljine ekvivalenta vode. Pomoću ovih merenja napravljene su kalibracione krive za snop jona helijuma pri različitim energijama.

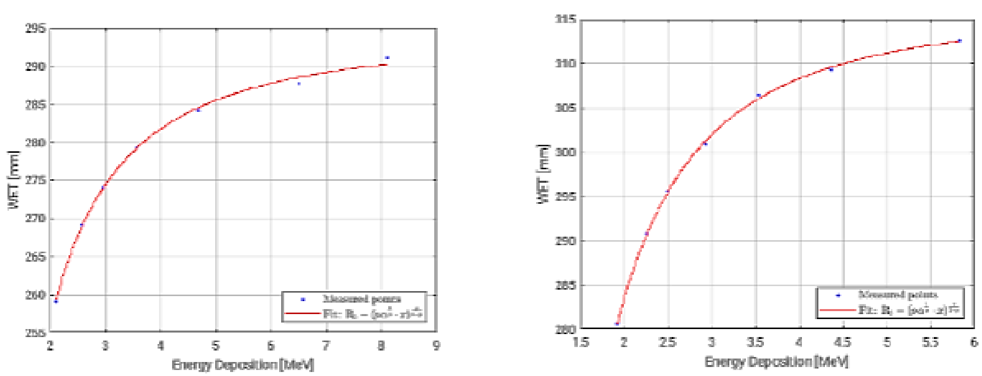

(a) 229.1 MeV/u (b) 239.5 MeV/u

Slika 6: Kalibracione krive koje omogućavaju pretvaranje izmerene deponovane energije u debljinu vodenog ekvivalenta (WET) za dve energije jona helijuma korišćene u eksperimentima.

Fantom korišćen u eksperimentima je napravljen od ljudskih kosti i obložen materijalom koji je ekvivalentan ljudskom tkivu.

Prikupljeni podaci tokom merenja su kasnije obrađeni kako bi se u obzir uzeli samo signali nastali od jona helijuma, a odbacili signali koji potiču od sekundarnih fragmenata ili neželjenih detektorskih artefakata.

Rezultati

Za dobijanje radiografa antropomorfnog karličnog fantoma ubrzanim jonima helijuma korišćene su energije od 229.1 MeV/u i 239.5 MeV/u. Regija od interesa je podeljena na devet manjih kvadratnih regija veličine 14 mm x 14 mm što je ujedno i veličina aktivnog sloja detektora. Fantom je pomeran u dva pravca normalna na pravac snopa, dok su detektori bili fiksirani kako bi se snimio radiograf načinjen od devet manjih radiografskih slika.

Prvo su rađena merenja za poravnanje šest detektora sa snopom ubrzanih jona helijuma. Prolaskom snopa jona kroz detektore moguće je dodatno poravnjanje detektora prema snopu jona. Rezultati dodatnog poravnjanja u dva pravca normalna na pravac snopa sa dve energije snopa su prikazani u tabeli 1, a detektor #3 je korišćen kao refentna tačka.

Coorection in direction [mm]	#1	#2	#3	#4	#5	#6	Energy
x	-8.4211	-9.4735	0	-0.0986	-0.3144	-0.3788	229.1
y	1.2236	0.0563	0	-2.1497	5.8294	6.7310	
x	-8.4702	-9.4993	0	-0.0999	-0.3217	-0.3780	239.5
y	1.5466	0.5763	0	-2.1456	5.8327	6.7112	

Tabela 1: Rezultati merenja za dodatno poravnjanje detektora.

Nakon merenja za poravnanje detektora rađena su merenja za dobijanje radiografa regije od interesa. Nakon obrade podataka dobijenih merenjem, otklonjeni su ‘’lažni’’ signali i za formiranje slike su koršćeni samo signali nastali od jona helijuma iz snopa. Putanja jona je rekonstruisana pomoću dva algoritma i ta dva radiografa su prikazana na slikama 7 a i 8 a. Radiograf prikazuje mapu debljine vodenog ekvivalenta (WET) i na kraju je upoređen sa digitalno rekonstruisanim radiografom od rendgenskog CT-a.

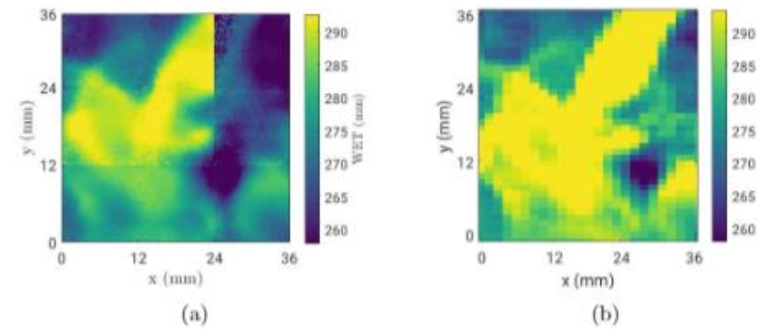

Slika 7: Poređenje radiografa dobijenog algoritmom - rekonstrukcije duž putanje (Along Path Reconstruction) (a) i digitalno rekonstruisanog radiografa (b).

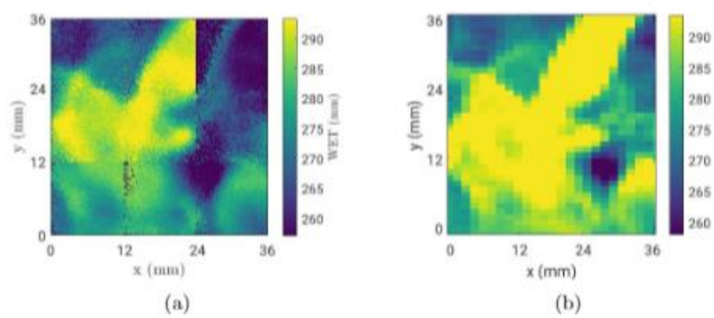

Slika 8: Poređenje radiografa dobijenog algoritmom rekonstrukcije putanje jona – *Cubic Spline Path* (a) i digitalno rekonstruisanog radiografa (b).

Radiograf dobijen algoritmom – rekonstrukcija duž putanje ima bolji odnos kontrasta i šuma (CNR, *contrast to noise ratio*), dok radiograf rekonstruisan algoritmom – Cubic Spline Path ima bolju prostornu rezoluciju.

Zaključak

Radiograf dobijen ubrzanim jonima helijuma omogućava preciznije određivanje debljine ekvivalenta vode od metode koja se najčešće koristi a to je CT simulator. Predstavljena studija pokazala je prednost ove metode i njegove prve primene na antropomorfnom karličnom fantomu. Prvi pokušaj primene postupka kalibracije za radiograf antropomorfnog fantoma nije u potpunosti uspeo. To znači da problem usaglašavanja debljine vodenog ekvivalenta sa slika dobijenih različitim energijama moraju biti dodatno istražena, a kalibraciona kriva mora biti verifikovana u dodatnom merenju. Za potencijalnu kliničku primenu metode radiografa ubrzanim jonima helijuma potrebna su dalja usavršavanja.

Quantitative helium-beam radiography of an anthropomorphic pelvis phantom

Contents

1 Introduction

The use of ionizing radiation (radiotherapy) plays an important role in the treatment of malignant tumor, in addition to other methods such as chemotherapy or surgery. The aim of radiotherapy is to provide sufficient dose to kill the tumor cells. In theory, an ideal irradiation delivers a defined dose distribution within the tumor and no dose outside it. In practice, it is impossible to spare all healthy tissue from irradiation, but the intention is to minimize the dose in it, in order to reduce adverse side effects.
Ion-beam radiotherapy was first proposed by Robert Wilson (1946) who realized that accelerated protons and heavier ions have enough energy to penetrate the human body, and could be used for cancer therapy. The first clinical use of a proton beam and subsequently a helium ion beam with an energy of 910 MeV took place at Berkeley in 1954 [1]. Today ion-beam [1] radiotherapy has a growing interest in cancer treatment. Currently, there are more than 75 facilities in operation worldwide and 40 facilities are being constructed with expected treatment start before 2021 [2]. By the end of 2018, 221528 patients have been treated with ions [3].
Protons and heavier ions (e.g. ^{4}He, ^{12}C) compared to photons have a superior depth-dose distribution. This distribution is common to all ions, and is called *Bragg curve*. A Bragg curve has a sharp peak of dose deposition at the end of the ion range, called *Bragg peak* [4]. This results in better sparing of healthy tissue surrounding the tumor, since the position of the Bragg peak in depth can be adjusted to the depth of the tumor by changing the initial energy of ions.
However, positioning the Bragg peak inside a target can be challenging. In order to predict the position of the Bragg peak, the ion energy loss (or stopping power (SP)) has to be known in the tissue through which the ions must pass. This is still a problem facing any ion-beam therapy today. Cormack in 1963 [5] was the first who realized that the energy loss of ions passing through a patient can tell us about ion stopping power inside the patient - something we can never get directly from X-rays. X-ray computed tomography (CT) is used for treatment planning purposes, not just for outlining structures, but also for measuring electron density maps which are used to calculate the dose deposition. The conversion of electron density to ion stopping power leads to an uncertainty in relative stopping power [2] (RSP). For protons this uncertainty is estimated as 1.6% for soft tissue, 2.4% for bone and 5.0% for lung [6].
Ion-beam radiography (iRAD) allows direct measurement of the object's integrated relative stopping power along the direction of the imaging beam [2]. This approach requires high-speed ion tracking before and after the patient and residual energy measurement or a connected quantity of the ions leaving the patient. With the range information the correct positioning of the patient relative to the beam an the correct prediction of the patient anatomy could be verified [7]. This method can be used to improve the treatments planned on converted CT

[1] The term ion includes protons and heavier ions.
[2] The relative stopping power of a material is defined as the ratio of the stopping power in this material to the stopping power in water.

images. However, currently iRAD is not used routinely, primarily because most of these experimental prototypes are bulky, expensive and difficult to adopt into the clinical environment [8].
The aim of this thesis was to further develop a method of helium-beam iRAD (αRAD) for the first application on an anthropomorphic pelvis phantom and in the end to compare WET values from the αRAD with the corresponding digitally reconstructed radiography (DRR) based on the planning X-ray CT.

1.1 Ion-beam radiotherapy

Radiotherapy with protons or heavier ions (ion-beam radiotherapy) provides several advantages over the conventional photon radiotherapy. The main advantage of using proton and heavier ion beams for radiotherapeutic patient treatment is the possibility to deliver a dose highly localized to the target volume. Healthy tissue around the target volume can therefore be largely spared from irradiation (figure 1). This is especially important when organs at risk (e.g. optic nerves) are located in the vicinity of the target volume. In addition, heavy ions projectiles exhibit an increased biological effectiveness in the Bragg peak caused by the dense ionization resulting in reduced cellular repair in tumor region [9]. The other advantage is that ion beam can be precisely controllable in three dimensions. With ions it is possible to produce a tightly focused pencil beam that is deflected laterally by two magnetic dipoles. Therefore, the tumor volume can be easily covered by deflecting the ion beam through magnets, which is not applicable for photon and neutron beams [10].

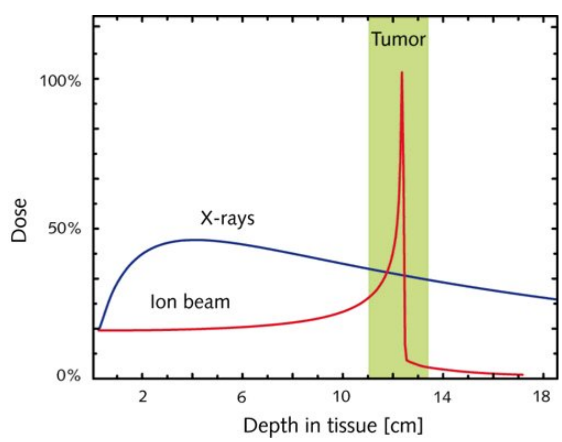

Figure 1: Comparison of the radiation dose as function of the depth in tissue for X-rays (conventional radiotherapy) and ion beam (ion-beam therapy). Reprinted from [11].

At the same time, the high gradient of the dose profile is a challenge as it makes ion-beam therapy more sensitive to uncertainties than the smaller gradient of photon radiotherapy. Figure 2 demonstrates the effect of an anatomical change on the dose distribution for ion-beam and X-ray radiotherapy. There are several reasons for ion beam range uncertainties. They might originate in the planning phase during the conversion of X-ray CT numbers to relative stopping power (RSP) of the tissue. They can also occur in the treatment phase due to changes in the spatial RSP distribution. These changes are mainly caused by anatomical changes (e.g. weight change or tumor shrinkage) or uncertainties in the patient set-up [2].

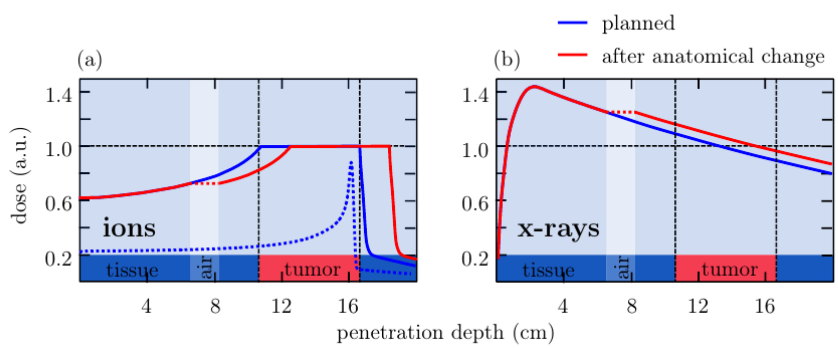

Figure 2: Comparison of depth-dose profiles before (blue solid lines) and after an anatomical change (red solid lines) for (a) ion-beam radiotherapy and (b) X-ray radiotherapy. The blue dotted line presents a pristine Bragg peak. Reprinted from [2].

1.2 Ion-beam radiography

Ion-beam radiography (iRAD) could improve the quality of ion-beam therapy. The major benefit of iRAD is the possibility to directly measure the **integrated relative stopping power**. A second potential advantage of iRAD is that imaging irradiation and the treatment irradiation can be performed with the same ion, which would completely avoid conversion errors. iRAD could also provide a quick verification of the patient set-up immediately prior to the ion-beam radiotherapy, with low radiological dose.
Energies required for iCT or iRAD are higher than those used in ion-beam radiotherapy. A reason for that is that a position of the Bragg peak must be located not in the patient, but in the detector behind the patient. Therefore, ions must have an energy sufficient to traverse the imaged object. For thick anthropomorphic pelvis phantom energies higher than the therapeutic energies (above 220 MeV/u that corresponds to a range of approximately 30 cm in water) were required. A first version of this energies (229.1 MeV/u and 239.5 Mev/u for ^{4}He ions) were recently implemented at the Heidelberg Ion-Beam Therapy Center (HIT) enabling for the first time iRAD of an anthropomorphic phantom with a WET exceeding 280 mm WET.

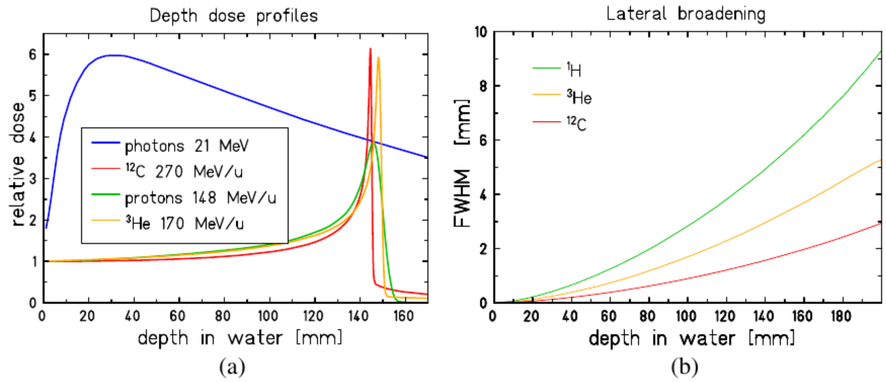

Figure 3: Depth dose profiles (a) and lateral broadening (b) of different ions.

After the ions crossed the object, the residual range or residual energy information is acquired. With this data, the integrated stopping power of the object can be determined. A radiograph is obtained from information about the energy, scattering, or attenuation of an ion beam exiting the object [2].
The heavier the ion is, it suffers less scattering in the imaged object (figure 3, b). Hence, helium iRAD gives better spatial resolution without any disadvantage in terms of dose compared to proton iRAD. The spatial resolution of helium iRAD is twice as good as for protons and for carbon ions is approximately 1.8 times better than for helium. Also, helium ions require much less energy to fully penetrate the object compared to the carbon ions (figure 3, a). On the other hand, heavier ions suffer from substantial nuclear fragmentation. Using carbon ions instead of helium would improve spatial resolution at the cost of higher doses [12]. Considering all of this, helium ions have been chosen for developing an αRAD of the pelvis phantom presented in this thesis.
Since the WET measured by αRAD has the same validity as WET measured by proton and carbon beams, αRAD can be applied as an image-guidance tool for proton, carbon or helium-ion therapy. The main advantage of the iRAD is that it can be performed right before the ion-beam therapy with the same positioning of the patient. The idea is to compare the iRAD WET map with the software reconstructed WET from planning X-ray CT. Differences in this two radiographs would mean uncertainties in the patient positioning or anatomical changes in the patient geometry.

2 Physical Background

This chapter reviews the physical background for the research presented in this thesis. The first part of the chapter examines the interactions of ions with matter in section 2.1. Furthermore, physical properties as Bragg curve, LET, dose and water equivalent properties are defined in section 2.2. Eventually, there is a brief introduction to semiconductor detectors in section 2.3 and description of two quantities for image quality characterization in section 2.4.

2.1 Interactions of Ions with Matter

In distinction to the indirectly electromagnetic radiation, ions are directly ionizing [13]. These particles lose their energy by ionizing the atoms of the material and eventually come to rest. Ions travelling through the material undergo interactions with electrons and the nuclei of surrounding stationary atoms. For the clinical energy range (up to 500 MeV/u) the contribution of bremsstrahlung and Cerenkov radiation, is very small and can be neglected. Ions slow down by multitude collisions with atomic electrons. Through collisions with a nucleus, they are deflected. Sometimes they have a head-on collision with a nucleus, producing secondary particles in motion. These three process are called *stopping*, *scattering* and *nuclear interactions*. Stopping and scattering occur via Coulomb interactions with atomic electrons and nuclei, while nuclear interaction with nuclei occurs via strong nucleon-nucleon force [14].

2.1.1 Stopping

When ions passes through a medium, it loses its energy by transferring it to the electrons of the medium's atoms. The transferred energy can be enough to knock an electron out of an atom and **ionize** it, or it can leave the atom in an **excited**, non-ionized state.
As illustrated in figure 4, the rate of energy loss can be calculated by taking into account a mass (M) and charge (ze) of ion which passes close to a free electron. To simplify the calculation, we suppose that the ion is non-relativistic, $v << c$, and that $M >> m_e$, where v and M are velocity and mass of the ion, c is speed of light and m_e is mass of electron. Also, we assume that the electron is free and initially at rest. Then, the energy gained by the electron is:

$$\Delta E(b) = \frac{2z^2e^4}{m_e v^2 b^2} \tag{1}$$

where b is the distance between ion and atomic electron. Let n be the density of electrons, then the energy lost to all the electrons located at a distance between b and $b + db$ in a thickness dx is:

$$-dE(b) = \Delta E(b) n dV = \frac{4\pi n z^2 e^4}{m{v_e}^2} \frac{db}{b} dx \tag{2}$$

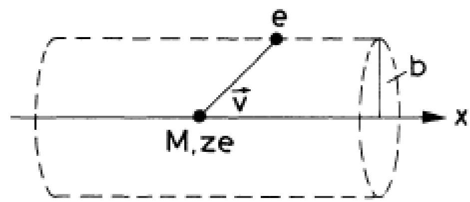

Figure 4: Collision of a heavy ion with an atomic electron. Reprinted from [15]

According to Bohr's classical case calculation the overall energy loss by collisions calculated by integrating over the range of the impact parameter is:

$$-\frac{dE}{dx} = \int_{b_{min}}^{b_{max}} \frac{4\pi n z^2 e^4}{m v_e{}^2} \frac{db}{b} = \frac{4\pi n z^2 e^4}{m v_e{}^2} \cdot \ln(\frac{b_{max}}{b_{min}}) \tag{3}$$

Bohr's classical formula gives a description of the energy loss for heavy ions, but for lighter ions (e.g protons) the formula breaks down because of quantum effects. The correct quantum-mechanical formula is called Bethe-Bloch formula:

$$-\frac{dE}{dx} = \frac{4\pi}{m_e c^2} \cdot \frac{n z^2}{\beta^2} \cdot (\frac{e^2}{4\pi\varepsilon_0})^2 \cdot [\ln\left(\frac{2 m_e c^2 \beta^2}{I \cdot (1-\beta^2)}\right) - \beta^2] \tag{4}$$

where c is the speed of light, ε_0 the vacuum permittivity and $\beta = \frac{v}{c}$ [14].

Energy loss per unit path length, $-\frac{dE}{dx}$, is numerically equal to the *stopping power* of the material. **Stopping power** (S) is defined as the retarding force acting on ions, due to interaction with matter, resulting in loss of particle energy [16]. It depends on the energy of the particle and on the stopping material. Materials with high atomic number have less stopping power than materials with small atomic number. The total stopping power (S_{tot}) is made up of three components[17]:

$$S_{tot} = -(\frac{dE}{dx}) = -[(\frac{dE}{dx})_{nuclear} + (\frac{dE}{dx})_{electronic} + (\frac{dE}{dx})_{radiation}] \tag{5}$$

The electronic (collision) stopping power is given by Bethe-Bloch formula (4). The elastic nuclear stopping power component is significant only for energies below $\approx$ 10 keV/u and therefore plays a role at the end of particle track [9]. Radiative energy loss due to bremsstahlung is negligible for particles much heavier than electrons. As a consequence of this, the stopping power of the ions at therapeutic energies is approximately equal to the electronic stopping power. Most of the ions in a monoenergetic beam travel the same distance, but not all experience the same number of collision. Therefore, their range is different and this phenomenon is called *range straggling*, or *energy straggling* if we focus on fluctuations in energy loss rather than range. Range straggling for heavier ions varies approximately inversely to the square-root of the particle mass (figure 5). This means that helium ions straggle 50% of the straggle of protons [10].

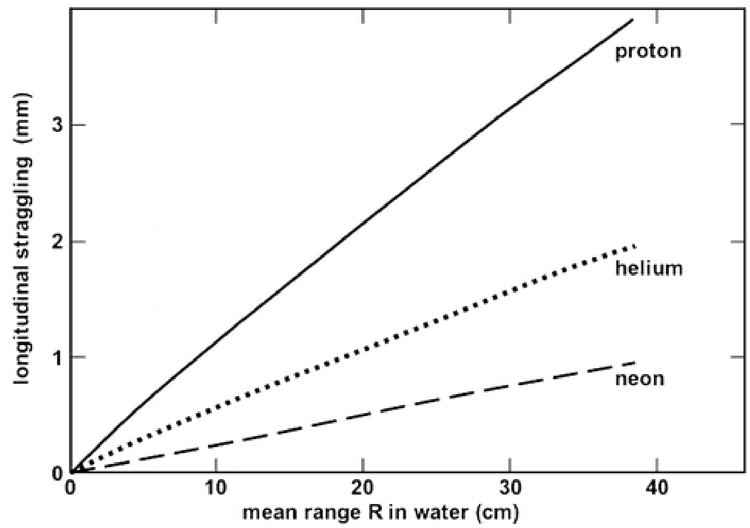

Figure 5: Comparison of proton, helium and neon beam straggling as a function of their path length in water. Reprinted from [10].

2.1.2 Scattering

When ions pass through the matter, they experience random deviations in their direction. This phenomenon, called *lateral scattering*, is predominantly caused by elastic Coulomb scattering from the nuclei of the target atoms, while scattering due to electronic interactions is neglected [6]. Since nuclei usually have a mass larger than the incoming ion, the transfer of energy is negligible, but the incoming particle's trajectory is diverted.
Single scattering is described by Rutherford cross section:

$$\frac{\mathrm{d}\sigma}{\mathrm{d}\Omega} = \left(\frac{1}{4\pi\varepsilon_0}\frac{Z_1 Z_2 e^2}{4E_0}\right)^2 \frac{1}{\sin^4(\frac{\theta}{2})} \tag{6}$$

where Z_1p and Z_2 are the charge of the projectile and target nucleus respectively, θ is the deflection angle and E_0 is kinetic energy of projectile. Even the deflection is small, the sum of all angle deflections lads to greater divergence of the beam after a thickness of material than incoming beam. This process is called **Multiple Coulomb Scattering** (MCS) and it causes a "zig-zag" path of the particles (figure 6).

Multiple Coulomb Scattering is described by Moliere distribution, but for small angles the higher order terms in Moliere's solution can be neglected and the angular distribution is approximated by a Gaussian function. For high energetic heavy ions, lateral scattering is smaller than for same particles with lower energies. Also, target materials made of heavy elements produce a large angular spread than targets containing light elements with the same thickness. The slight lateral deflection of heavy ions that pass through an absorber is an ad-

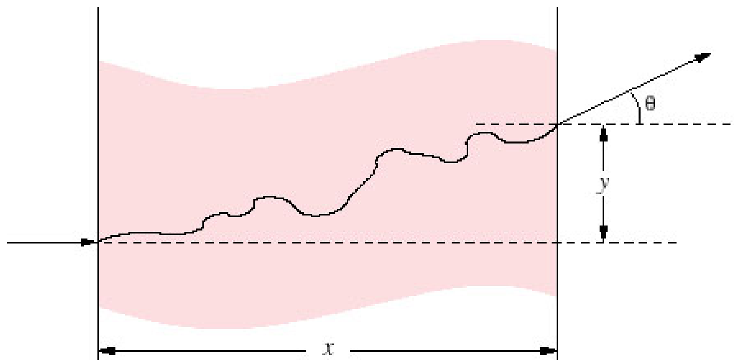

Figure 6: An illustration of a particle scattering through a material of thickness x resulting in a displacement of y and a scattering angle of θ. Reprinted from [18].

vantage of heavy ions compared to protons and it has a lead in radiotherapy by saving the healthy tissue around tumor[9].

2.1.3 Nuclear Interactions

Stopping mechanism of ions penetrating a thick absorber occurs mostly by collisions with atomic electrons, while the probability of nuclear reactions is much smaller, but has a significant contribution at large penetration depths. At energies of several hundred MeV/u, which are required for radiotherapy applications, nuclear reactions may result in partial fragmentation or in a complete disintegration of projectile and target nuclei [9].
Nuclear fragmentation process can be described by the abrasion–ablation model as illustrated in figure 7. Nucleons are abraded and form the hot reaction zone (fireball) in the overlapping area of the interacting projectile and target nuclei, while the outer nucleons (spectators) are only slightly affected by the collision. The remaining projectile, target fragments and the fireball de-excite by evaporating nucleons and light clusters in the second step (ablation). While the projectile-like fragments continue travelling nearly the same direction and velocity as the primary ions, the target-like fragments are emitted isotropically with much lower velocities. Nuclear reactions cause a loss of primary ions and a build-up of lower-Z fragments. The fragments have longer ranges than the primary ions, hence they increase penetration depth. The depth-dose profile of the heavy-ion beams therefore shows a characteristic fragment tail beyond the Bragg peak [19].
A benefit of nuclear fragmentation is the production of prompt gamma rays, prompt secondary ions and beta emitters, which are used in beam monitoring methods. Secondary ions are projectile fragments that are created in nuclear interactions. Beam monitoring based on tracking of prompt secondary ions is providing a real time information about ion beams.

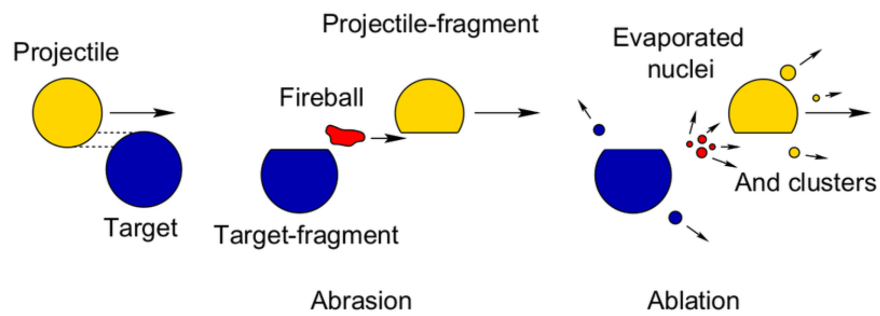

Figure 7: A simplified model of the nuclear fragmentation due to peripheral collisions of projectile and target nucleus. Reprinted from [19].

2.2 Physical Properties

In this chapter the most important physical properties of ion beams used in radiation therapy and ion-beam imaging are presented.

2.2.1 Bragg Curve

As a heavy particle slows down in matter, its kinetic energy changes so its rate of energy loss will change. More energy per unit length will be deposited towards the end of its path rather than at its beginning. This effect is known as a Bragg curve and it is presented in figure 8. The Bragg curve describes the energy loss of heavy ions during travel through matter. Also, it is the depth-dose profile for the heavy ion beam.

For this curve is typical the *Bragg peak*, which occurs immediately before the particles come to rest. By changing the kinetic energy of the incident ions, the position of this peak in tissue can be accurately adjusted to the desired depth. The Bragg peak can be fully explained by three physical processes described in section 2.1: stopping, scattering and nuclear reactions. As it can be seen in figure 8 most of the energy is deposited near the end of trajectory. Yet, at the very end, heavy ions start to peak up electrons and the $\frac{dE}{dx}$ (and dose) drops. This behaviour is used in radiotherapy to deliver high dose within a tumor, and to spare surrounding healthy tissue. Manipulations of the Bragg peak, such as spreading it out, plays an important role in heavy-ion radiotherapy. Quite narrow Bragg peak is spread in order to treat large tumors. The spread-out Bragg peak (SOBP), as a result of several stacked Bragg curves, covers the target (tumor) and spares the healthy tissue [15].

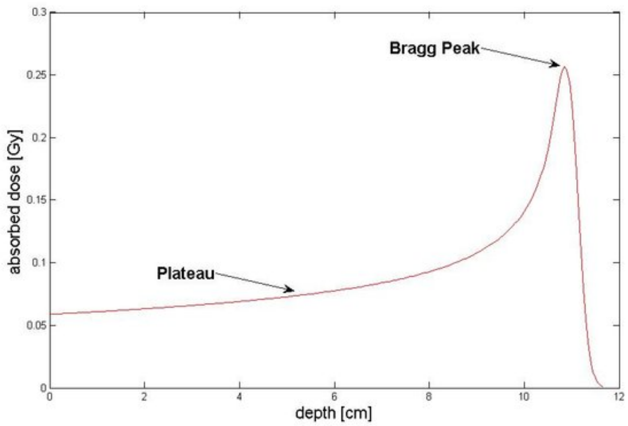

Figure 8: The Bragg curve: the absorbed dose of a monoenergetic proton pencil beam as function of the penetration depth. Reprinted from [20].

2.2.2 LET and RBE

The *linear energy transfer* (LET) is defined as the energy deposited by an ionizing particle travelling through matter per unit length of the track [22]. It is closely related to the stopping power described in section 2.1.1. However, the stopping power is a property of a material and describes energy absorbed by matter while LET describes the energy loss of the particle.
LET (commonly expressed in units of $keV/\mu m$) can not be used as a parameter to differentiate qualitatively the biological effects of different kinds of radiation because it is not a constant value. As a projectile ion's charge and energy change along the path of the particle, so does LET changes [10]. Even though LET is not a good parameter for defining the full spectrum of biological effects on radiation, it is still used to categorize damage caused by ions. For a given type of radiation, the LET goes down as the energy goes up. This means that a high-energy ion has a lower LET than the same low-energy particle [22]. The LET below 10 $keV/\mu m$ is considered as low LET radiation while above 10 $keV/\mu m$ is high radiation [23]. Heavy ion beams find a medical application due to the high LET value within the Bragg peak and low LET value in the entrance channel of their trajectory. Since cells have less ability to repair high-LET radiation damage, high-LET radiation is more effective for killing tumors.
Relative biological effectiveness (RBE) is defined as as the ratio:

$$D = \frac{D_{ref}}{D_{rad}} \tag{7}$$

where D_{rad} is the dose released by the radiation, and D_{ref} is the dose released by a reference radiation that produces the same amount of biological damage. Thus, the RBE depends on the radiation type and energy, dose and the biolog-

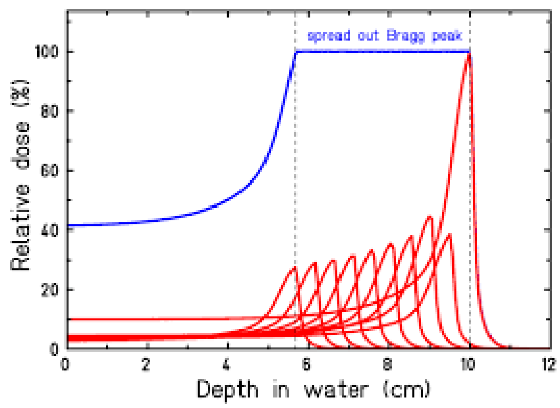

Figure 9: The superposition of Bragg curves (red) forms the SOBP (blue). Reprinted from [21].

ical endpoint.
The RBE is very important quantity in treatment planning of heavy-ion therapy, as it determines the photon-equivalent dose. The photon-equivalent dose defines the conventional radiation dose which would create the same biological effect as the radiation applied.
The heavy ion beams, as they travel through the matter, show very diverse RBEs. Also, different ions of the same LET may have different RBEs. The damage caused by radiation to a living cell is determined primarily by its location. The most critical is the damage to the cell nucleus, especially the DNA molecules placed inside, which can lead to cell death or mutation. DNA damage has two pathways: direct ionization of its components or indirect damage through the water radiolysis in the particle track. The direct damage is more relevant for the high-LET radiation, since it has denser tracks than low-LET radiation [24]. As shown in figure 10 with LET, RBE increases to a maximum value depending on ion type and decreases with higher LET values [9]. The reason for the decrease of RBE is that the more energy radiation does not change the outcome. This is so called "overkill" effect.

2.2.3 Dose

The most important physical quantity in radiotherapy is the dose deposited in tissue, called *absorbed dose*. It is defined as the mean energy dϵ per unit mass dm deposited by ionizing radiation [25]:

$$D = \frac{d\epsilon}{dm} \; [Gy = 1J/kg] \tag{8}$$

Depending on the nature of the radiation and the type of tissue or organ exposed, the energy released in a living organism by radiation causes different effects. Hence, *the biological dose* is used, which is absorbed dose multiplied

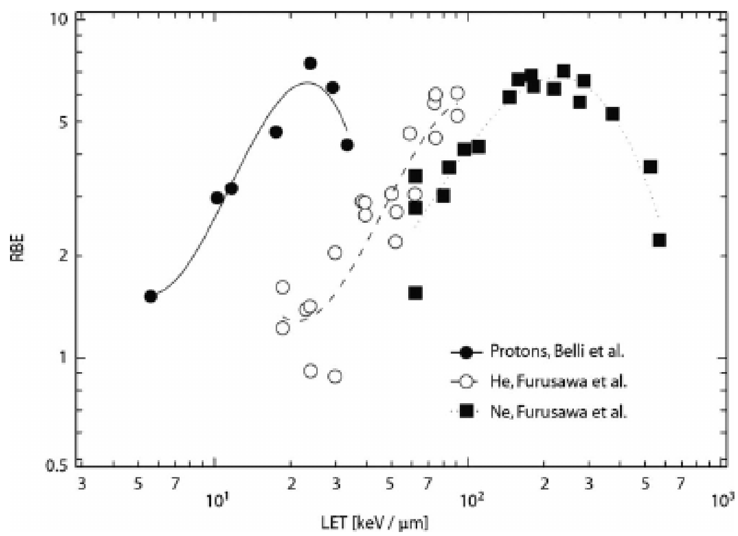

Figure 10: Dependance of RBE on LET and particle type. Reprinted from [9].

by a weighting factor (RBE) depending on the nature of the radiation. Ion Beam Therapy treatment planning is a balancing act between protecting critical organs at risk from high-dose irradiation (e.g., spinal cord, optic nerves) and avoiding tumor underdosage. Water is used as a reference tissue medium in radiation therapy. Dose measurements are usually performed by air-filled ionization chambers and must be converted by correction factors to the absorbed dose in water [10]. The ratio of the Bragg peak dose versus dose in the entrance region is larger for heavy ions compared to protons. Also, heavy ions has a larger RBE in the Bragg peak compared to the entrance region. Although, this advantage is not valid for very heavy ions (above oxygen), because for them RBE is already high in the entrance region and does not increase much more in the Bragg peak. In addition, due to their larger mass, lateral and range straggling is smaller for heavy ions as compared to protons. With lighter-ion beams, the dose of radiation falls rapidly beyond the Bragg peak protecting from harmful radiation healthy tissues located downstream of the target. For heavier ions this tail region is higher because of the increase of nuclear fragmentation process.

2.2.4 Water Equivalent Properties

An accurate value for the range of heavy ions along the beam axis is very important. This value depends on the target material parameters, as well as on the charge number and energy of the projectile ion. In order to compare these quantities, they must be referred to the same material. Because of its similarity to soft tissue, water has been chosen as the reference material.

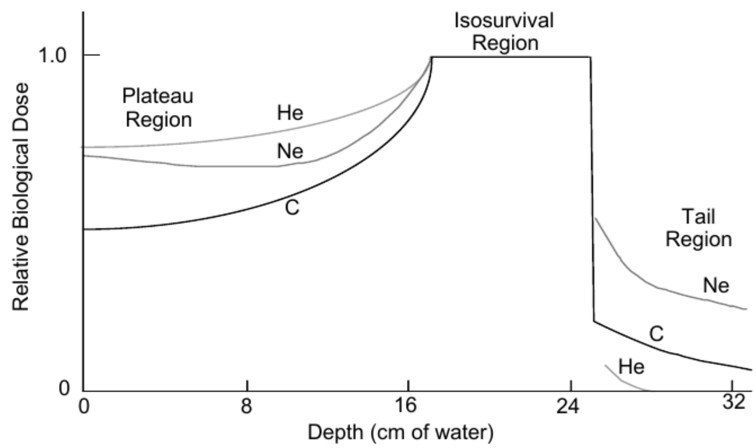

Figure 11: The relative biological doses of SOBPs of helium, carbon, and neon ion beams as a function of penetrating depth in water are shown for comparison. Reprinted from [26].

Water equivalent thickness (WET) is defined as thickness of water that causes the same energy loss of a beam as it would lose in some other medium [27]. In other words,the WET of the material is the thickness of water that results in the same range. The equation to calculate WET for heavy ion beams is:

$$WET = t_w = t_m \frac{\overline{S}_m}{\overline{S}_w} \tag{9}$$

where t_w and t_m are thicknesses of water and target material; $\overline{S}_w$ and $\overline{S}_m$ are the mean values of stopping power for water and the material, respectively.

2.3 Basics of Semiconductor Detectors

The Timepix detector is a semiconductor detector, also called solid state detector. A semiconductor detector is a detector that has a detection medium made of semiconductor substance, for instance, silicon or germanium crystal. The detection medium transforms the energy deposited by a particle to an electrical signal. Particle energy is absorbed by semiconductor material producing mobile charge carriers (electron-hole pairs).

Semiconductor materials have an electrical conductivity value between conductors and insulators. Their conducting properties may be changed in useful ways by adding impurities into the crystal structure. This procedure is called *doping* and doped semiconductor material is called *extrinsic semiconductor*. The extrinsic semiconductor doped with electron *donor* atoms is classified an **n-type** semiconductor since *negative electrons* are the majority of charge carriers in the crystal. Extrinsic semiconductor doped with electron *acceptor* atoms is called a **p-type** semiconductor because the majority of charge carriers are *positive holes*.

If the atomic number of the semiconductor is Z, then the dopant of atomic

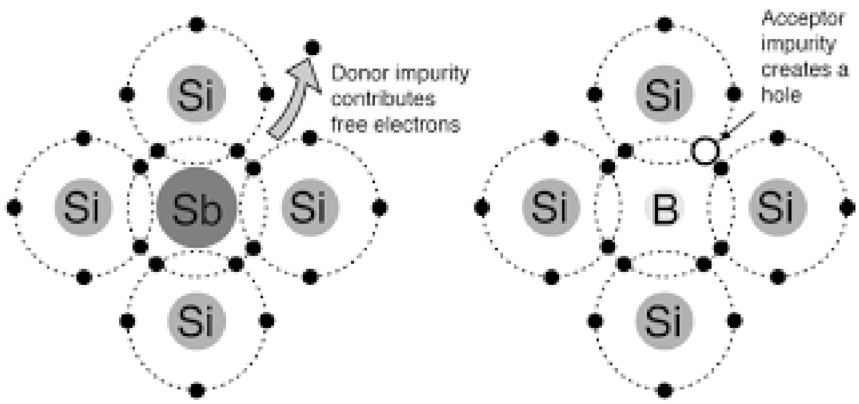

Figure 12: Schematic illustration of n-type (left) and p-type (right) semiconductor.

number Z+1 has one electron lightly bound and little thermal energy is enough to excite it to the conduction band. Electrons in conduction band are available mobile charge carries. If the atomic number of the dopant is Z-1, one of the bonds lacks an electron. Little energy is enough to "catch" a neighboring atom's electron. In this way, the unfilled bond (a hole) moves like a positive mobile charge [28].
A p–n junction is a boundary or interface within a single semiconductor crystal between two types of semiconductor materials, n-type and p-type. Near the junction, the n-type material electrons diffuse across the junction, combining with holes in p-type material. An insulating region where the mobile charge carriers have been diffused away is called *depletion region*. The result of the electron diffusion is an electric field which limits the thermal diffusion. This separation of charges at p-n junction produces a potential barrier which must be overcome by an external voltage source to allow the junction conduct.
When a voltage is applied with negative polarity on the n-type and positive polarity on the p-type semiconductor (*forward bias*) electrons and holes diffuse toward the junction. When a voltage is applied opposite (*reverse bias*), carries are attracted away from the junction and depletion region is thicker (figure 13). The depletion region of the p-n junction is used as a sensitive area of the semiconductor detectors. In the case of reverse bias, the natural potential difference that occur upon contact of the two sides of the junction is significantly enhanced and the depletion region thickness is increased. This means, the semiconductor detector operates much better if an external voltage is applied in the reverse biased direction.
In semiconductor detectors, ionizing radiation produces electron-hole pairs which are proportional to the energy of the radiation. Compared to the energy required to produce paired ions in a gas detector, the energy required to produce

electron-hole pairs is very low. Therefore, the energy resolution in semiconductor detectors is higher.

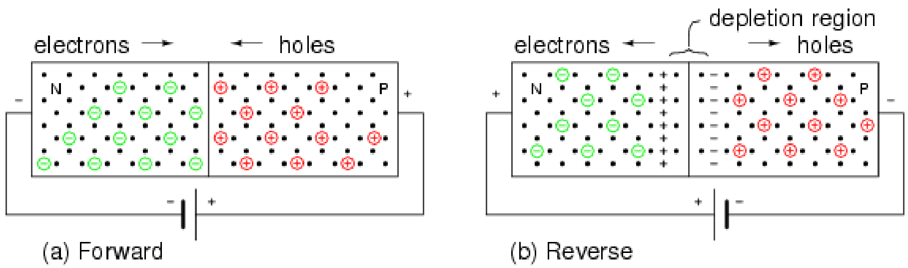

Figure 13: Schematic illustration of forward (a) and reverse (b) biased p-n junction.

2.4 Quantities for image quality characterization

In this section, two quantities used to compare images quantitatively are defined. They are used to compare iRAD images (presented in results, chapter 4) produced by two different reconstruction algorithms.

2.4.1 Spatial Resolution

Spatial resolution (SR) of an image is defined as the maximum number of line pairs per unit length distinguishable in that image.

2.4.2 Contrast to noise ratio

Contrast to noise ratio (CNR) is defined as possibility to distinguish different intensity values in an image:

$$CNR = \frac{|\langle S_1 \rangle - \langle S_2 \rangle|}{\sqrt{\sigma_{S1}^2 + \sigma_{S2}^2}} \tag{10}$$

where, $\langle S_i \rangle$ and σ_{Si}^2 are the mean and the standard deviation of pixel values in two homogeneous region of the image [29].

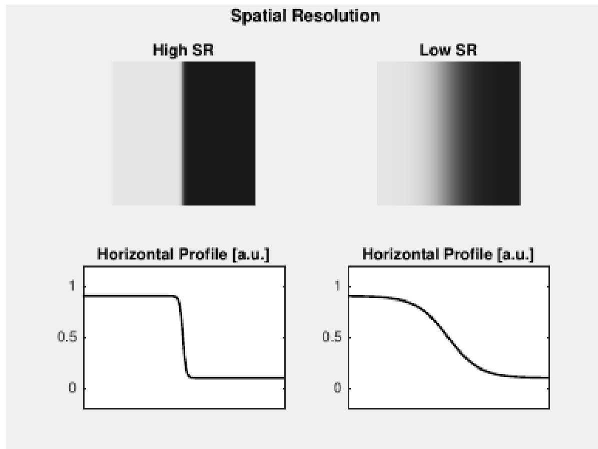

Figure 14: Example of an image with high SR (left) and low SR (right). Corresponding horizontal profiles are shown in the lower panels. Reprinted from [29].

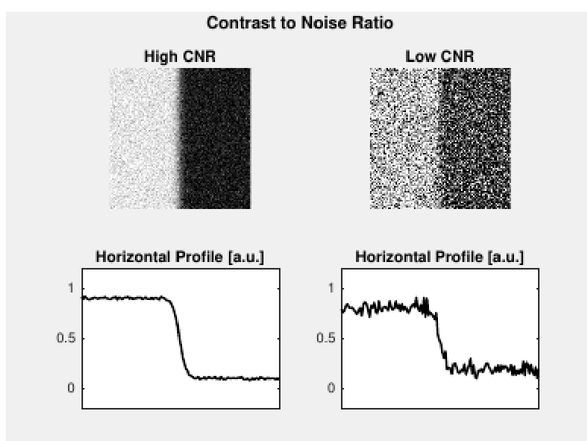

Figure 15: Example of an image with high CNR (left) and low CNR (right). Corresponding horizontal profiles are shown in the lower panels. Reprinted from [29].

3 Materials and Methods

This chapter describes the materials and methods which were used to perform the measurements of the thesis. The experiments were carried out with multiple Timepix detectors at the Heidelberg Ion-Beam Therapy Center (HIT), which is described in section 3.1. Furthermore, this chapter presents the Timepix detectors, their capabilities and operating modes in section 3.2. Eventually, the experimental set-up and data processing are described in section 3.3 and 3.5.

3.1 Heidelberg Ion-Beam Therapy Center (HIT)

The Heidelberg Ion-Beam Therapy Center (HIT) is the first European facility for radiotherapy with proton and carbon ions [30], and has started operation in 2009. It contains three treatment rooms and one experimental room. Two rooms are equipped with horizontally fixed beamlines for the patient treatments and one with a 360° rotating gantry, so the beam may be directed to the patient from arbitrary directions [31]. In addition to protons (^{1}H) and carbon (^{12}C) ions, used in clinical practise, helium (^{4}He) and oxygen (^{16}O) ion beams are available in the experimental room. All the experiments presented in this work were performed in the experimental room with the fixed horizontal beamline.

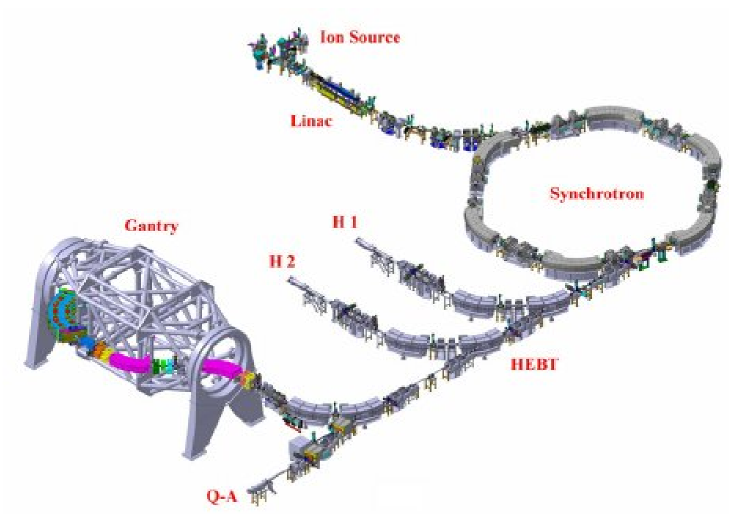

Figure 16: Overview of the accelerator at HIT facility. Two patient rooms with horizontally fixed beamlines (H1, H2), one room with 360° rotating gantry (Gantry) and the experimental room (Q-A) are shown.
Reprinted from [31].

The beams mentioned above are provided by a linac-synchrotron system. Protons are produced using hydrogen gas, while carbon dioxide is used for producing carbon ions. Once the ions of interest are produced they are pre-accelerated in a linear accelerator. This is where the ions are accelerated up to 10% of the speed of light. The pre-accelerated ions are then injected into the synchrotron where they can be accelerated to 255 discrete energy steps, corresponding to the range of 20 mm to 300 mm in water [31]. An advantage of using a synchrotron as accelerator for cancer radiotherapy is that it can accelerate ion beams to various energies [32]. After extraction of the beam from the synchrotron, ions are directed to the treatment rooms via the high energy beam transport system. Dipole magnets deflect the beam, while quadrupole magnets are used to focus the beam for the treatment.

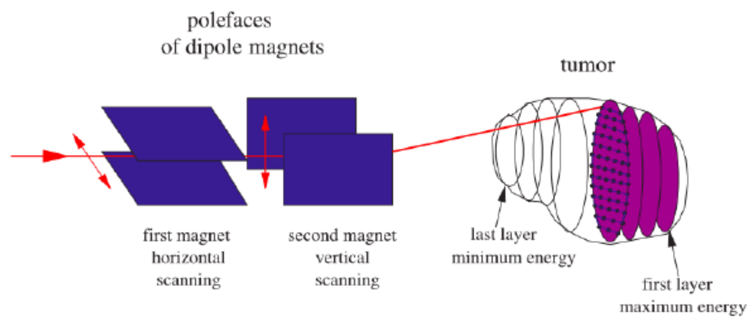

Figure 17: The rasterscan technique at HIT. Reprinted from [24]

The tumor volume is covered by pencil beams. Active volume scanning in three dimensions is achieved by magnetic deflection of the beam in lateral direction (rasterscan technique, figure 17) and by energy variation of the synchrotron which provides coverage of different depths in order to fully cover the target volume [33]. This method allows very high dose conformity since the beam is actively controlled in longitudinal and lateral direction [34].
In the beam nozzle at HIT, behind the vacuum exit window of the accelerator is the beam application monitoring system (BAMS, Siemens AG) [35]. It is made up of two multi-wire proportional chambers (MWPCs) and three ionization chambers (ICs). It gives a real time position and fluence of the beam.

3.2 The Timepix Detector

The Timepix[3] detector is a semiconductor pixel detector developed by the Medipix2 Collaboration at CERN [36]. It is a hybrid detector, which means that a sensitive sensor is coupled with an electronic chip. It has detection efficiency close to 100% for heavy ions.
A sensitive area of the detector is 14 mm x 14 mm divided into 256 x 256 pixels with a size of 55 μm x 55 μm. This sensitive layer is made of 300 μm thick crystalline silicon and bump-bonded to the readout chip pixel-by-pixel [37]. It is a silicon n-type semiconductor with a donor concentration of approximately (0.34$\pm$0.09) x $10^{12} cm^{-3}$. Each pixel has its own electronics and circuity, which enables the independent settings and operation for each pixel.

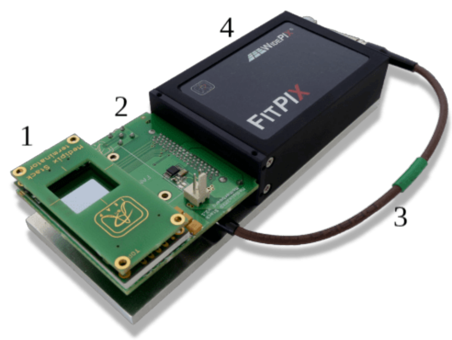

Figure 18: Timepix detector (1) connected to the read-out interface (4), with motherboard (2) and bias voltage (3). Reprinted from [38].

The detector is attached to a motherboard, which connects the detector and the read-out interface (figure 18). More detectors can be piled up together and fixed to the same motherboard. When attached to the same motherboard, they are automatically synchronized, forming, a so called *stack* [39]. The read-out interface provides a reverse bias voltage that is applied to the sensor layer and an external clock frequency. It is connected to a personal computer via USB 2.0, where the detectors' parameters are controlled by the software *Pixet*. With this software it is possible to set operation mode, signal threshold, frame duration, clock frequency, bias voltage and many other settings [29]. The read-out interface collects the data in frames (figure 28). A frame is the time interval of data acquisition (*active time*). Between two frames is a *dead time* interval, during which the data are not acquired but processed before the beginning of the next frame. The interface allows achieving up to 90 frames per second with a single detector [39].

[3]The detectors were produced by ADVACAM s.r.o., Praha, Czech Republic

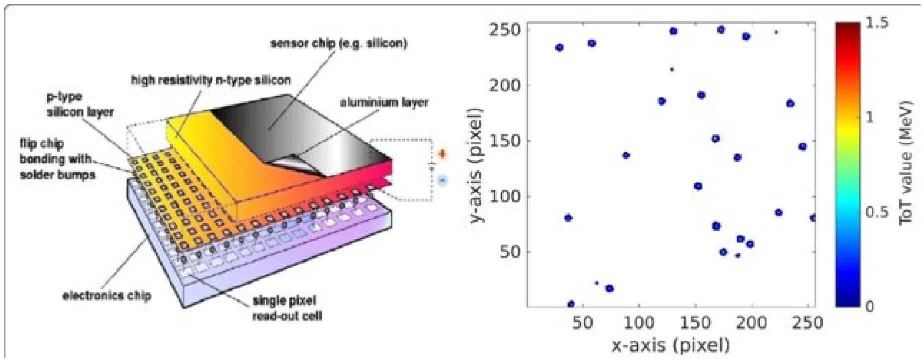

Figure 19: Left side: Visualization of a single Timepix detector structure. Right side: A frame example. Signal was recorded by the Timepix detector (operated in the energy mode) during helium ion beam imaging. [37]

3.2.1 Operating Modes

Each pixel can be operated in different modes. Four different operating modes are described in the following and presented in figure 20.

- **Medipix mode**: The Medipix mode or **counting mode** counts the number of events above the threshold. The counter value increases every time the output signal rises above the threshold. This enables counting the number of ionizing particles that hit a certain pixel during the acquisition time.

- **Time-over-Threshold (ToT) mode**: Time-over-Threshold (**energy mode**) measures the energy (collected charge) in each pixel, deposited by the ionizing particles. In this mode the counts increase continuously as long as the signal is above the threshold. The counts can be converted into deposited energy in a pixel applying an energy calibration. As each pixel has its own read-out circuit, this calibration needs to be performed for all the pixels.

- **Timepix mode**: The Timepix (**Time of arrival**) mode enables measuring the arrival time of the first event above threshold. When the incoming signal exceeds the threshold, the counts increase until the end of the acquisition time. This mode can be used for tracking of the particles, based on the measurement of the arrival time with 100 ns precision for an external clock frequency of 10 MHz that was used in this work.[37].

- **Masked mode**: This additional mode is used to deactivate damaged pixels.

In this thesis five detectors were operated in Timepix mode, and one was operated in Time-over-Threshold mode.

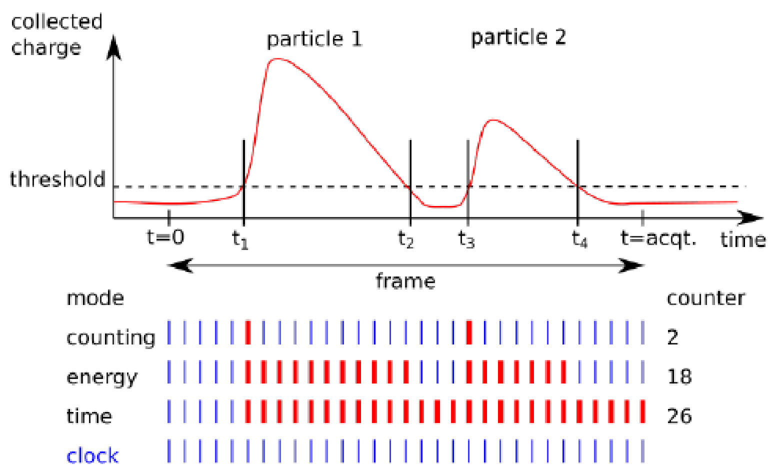

Figure 20: Schematic illustration of the different operating modes of the Timepix detector. Reprinted from [40].

3.2.2 Energy calibration of the Timepix detector working in ToT mode

The calibration procedure is based on the measurement of X-ray fluorescence [41]. X-ray fluorescence is the emission of a photon caused by electron transition in the electronic structure of an atom. The electron transition is induced by a photon and its effect is an emission of photons characteristic to the target material. Therefore, the result of X-ray fluorescence is the emission of monochromatic light which can be used for energy calibration of the detector. Photons are emitted isotropically, which enables positioning the detector (as shown in figure 21a) in order to avoid the primary beam to be detected.

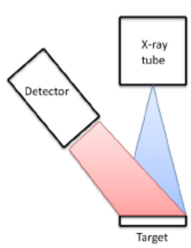

(a) Fluorescence set-up

Atom number	Materials	Abbreviation	Kα (KeV)	Kβ (keV)
28	Nickel	Ni	7.477	8.264
29	Copper	Cu	8.047	8.904
30	Zinc	Zn	8.638	9.571
40	Zirconium	Zr	15.774	17.666
46	Palladium	Pd	21.175	23.816
47	Silver	Ag	22.162	24.942
49	Indium	In	24.207	27.274
50	Tin	Sn	25.270	28.483

(b) Fluorescence targets with corresponding energies

Figure 21: Set-up for energy calibration of Timepix detector. This figure was reprinted from [42]

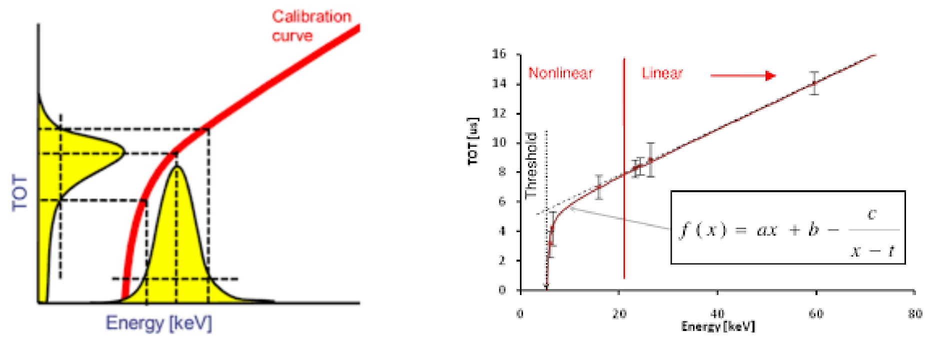

(a) Gaussian fit

(b) Dependence on particle energy of the ToT signal measured by single pixel, modeled by a surrogate function $f(x)$

Figure 22: The nonlinear calibration curve of a Timepix pixel device in ToT mode. Reprinted from [43].

In the calibration procedure, based on X-ray fluorescence, the detector is irradiated by monoenergetic radiation recording a spectrum for each pixel. The spectral peaks are then fitted with Gaussian functions. Fitting of spectral peaks with Gaussian functions gives shifted results in the region close to the threshold. This problem occurs due to nonlinear response of pixels in the energy range close to the threshold. The solution is fitting with a combination of a Gaussian and a surrogate function $f(x)$, depending on four parameters [43]:

$$f(x) = ax + b - \frac{c}{x - t} \tag{11}$$

To convert Time-over-Threshold value (TOT) into energy (E) it is needed to apply a set of calibration matrices a, b, c, and t. The matrices are the result of detectors' calibration. They carry the calibration values of each pixel, hence their size is 256 x 256 elements.
In the equation 11, x stands for the energy (in keV) deposited in the pixel, $f(x)$ is counter value , and a, b, c, and t are considered matrices.
Assuming a Gaussian energy distribution(figure 22a), the corresponding ToT output will be distorted by the non-linear function, producing a distorted Gaussian output distribution [44] At low energy, the ToT probability function can be fitted with a distorted Gaussian, but at high energy the ToT dependency of energy is close to linear (figure 22).
This calibration is just important for detector #5 out of 6. An accurate calibration of energy deposition is however very important, since this quantity determines the contrast of obtained radiographs.

3.3 Experimental set-up

In this section, the experimental set-up for alignment and iRAD measurements are described.
The experimental set-up is chosen with the aim to perform helium-beam radiography of an anthropomorphic pelvis phantom, based on energy deposition measurements. As shown in figure 23 a detection system is composed of six parallel Timepix detectors. Five of them (#1, #2, #3, #4, #6) operate in Time (Timepix) mode while one (#5) operates in Energy (ToT) mode.
The front tracking system contains two detectors (#1, #2) positioned in front of the phantom. This allows the position and direction of incoming ions to be determined.
The rear tracking system contains two detectors (#3, #4) positioned mounted behind the phantom to measure the outgoing ion position and direction.
Energy detection system contains the last two detectors (#5, #6). Detector #5 operates in Energy mode and measures the energy of upcoming ions. This detector is coupled with one detector operated in Time mode due to the lack of time information of the Energy mode.
Each pair of detectors is connected to a read-out interface and all the read-out interfaces are connected to the synchronization unit. This connection to one synchronization unit enables the tracking of ions over the setting.
The combination of energy deposition information and the trace of ions is used for the image formation.

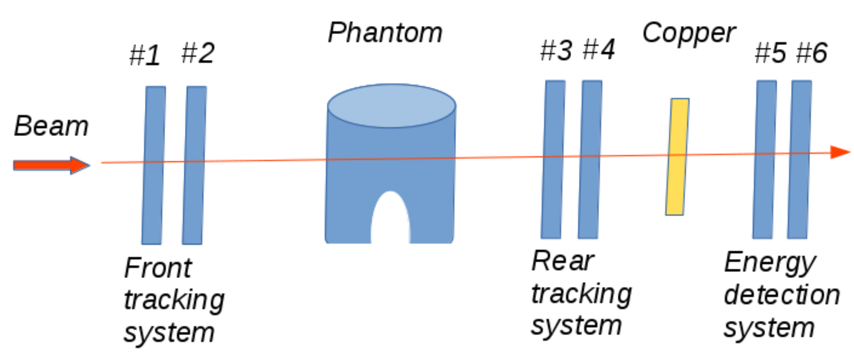

Figure 23: Schematic illustration of the experimental set-up.

3.3.1 Alignment measurements

A correct alignment of the six detectors is very important for this experiment. Adjustable metal construction was used to hold and position the detectors. Also, the laser system (with a precision of about 1 mm) at HIT facility was used in order to position the center of each detector on the beam direction. To increase the precision, additional measurements were performed to determine the residual misalignment of the detectors. The alignment measurements (figure 24) were performed with a helium ion beam, without any target (phantom) or BUM. The energies of the He ion beam used for alignment measurements were the same as for later performed αRAD of the phantom - 229.1 MeV/u and 239.5 MeV/u. The cluster position distributions were fitted with polynomial curve along the x and y directions, perpendicular to the beam axis (z). The maxima of the polynomial fits indicate the beam mean position. The beam mean position on the third (# 3) detector was used as reference and residual shifts of the other detectors were determined with regard to the reference. After performance of the alignment measurements the detectors were not touched in order to keep an identical positions of the detection system. Only the phantom and copper were added afterward for αRAD measurements.

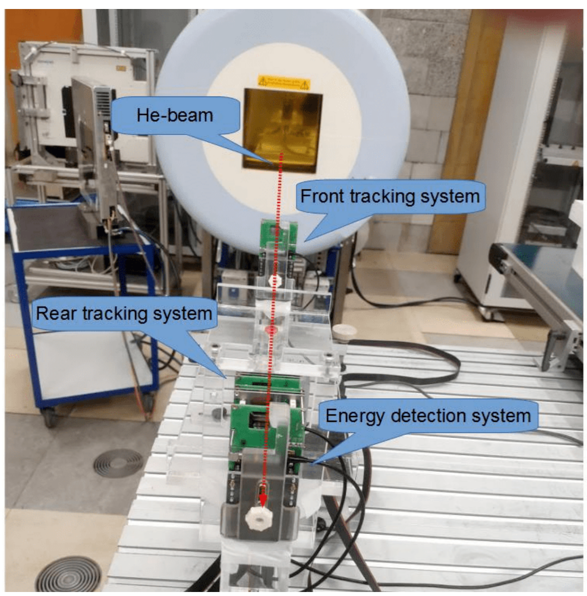

Figure 24: Experimental set-up for alignment measurements.

3.3.2 αRAD measurements

For the αRAD measurements, the pelvis phantom was positioned between front and back tracking system, and BUM was positioned between back tracking system and energy detection system (figure 25). The Alderson Radiation Therapy

Phantom used in this experiment is an anthropomorphic pelvis phantom, made from human skeletons consistent. The phantom soft tissue is molded of tissue-equivalent material and has the average density of human soft tissue.
A region of interest (ROI) was marked on the pelvis phantom and the phantom was positioned between detector #2 and #3 (figure 23). The region of interest is a square with dimensions of 36 mm x 36 mm, although the size of detectors used in this experiment is 14 mm x 14 mm and hence the largest size of an image that can produce. In order to produce larger αRAD image of the phantom, the phantom must be moved in x and y directions, perpendicular to the beam axis while the detectors are stationary. That is why the region of interest is divided into nine squares with dimensions of 12 mm x 12 mm, so it is possible for the detectors to produce nine images with overlapping edges 2 mm thick. This nine images were later compounded in one bigger image by using the overlapping edges for the alignment of the small radiographs. A 2D moving stage within the experimental room connected with a PC was used to automatically move the phantom in two directions in steps of 12 mm.

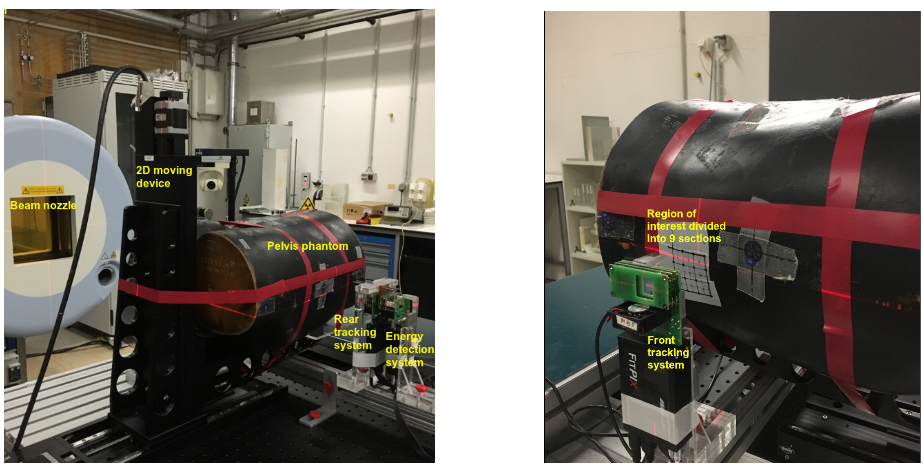

Figure 25: Experimental set-up for the αRAD measurements.

Ions traveling across the phantom and detectors undergo Multiple Coulomb Scattering (MCS), which causes a deviation from a straight line. Ions with higher energies suffer less Multiple Coulomb Scattering and allow better reconstruction of the path, which generate better spatial resolution of the final image. Also, higher energies decrease absorbed dose in the phantom/patient. For this reason, higher energies of the helium beam are preferred.
In order to achieve better WET resolution, the steepest rising part of the Bragg curve has to be positioned on the energy detector (#5). That is feasible by choosing the initial energy of the beam. The rising part of the Bragg curve is chosen because it shows a high difference in energy deposition for a little change of crossed WET.
To place the rising part of the Bragg curve on energy detector while using high

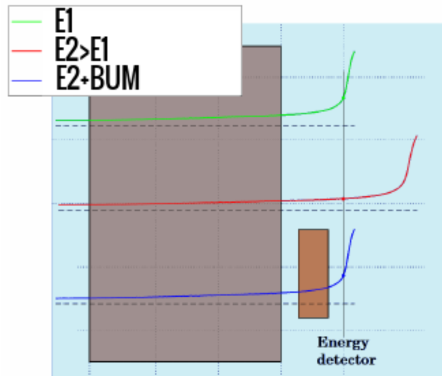

Figure 26: Schematic depiction of the function of the copper degrader (BUM). Modified from [29].

energy of the beam, an element called **the build-up material** (BUM) is used (figure 26). This element is made of copper and is set between the rear tracking system and energy detection system (figure 23) in order to absorbe the energy of the beam and degrade its range. The combination of a fixed BUM thickness and an adjustment of the initial energy assured that the position of the rising part of the Bragg curve is on the energy detector.

3.4 WET calibration

The thickness of the phantom is different for all the nine regions of interest and each region has different water equivalent thickness (WET) value. For each ROI the WET was estimated based on X-ray CT data. This has to be done in order to optimally adjust the initial energy of the beam. This process is the one currently used in the clinic with uncertainties of about 3%.
The aim of iRAD is to deliver a more accurate WET map of the ROI. For this purpose calibration curves for He beam at different energies, developed within the same research group, were used. In order to create these calibration curves that convert energy deposition to WET, several measurements at HIT with for different energies were performed. The set-up for those measurements consisted six Timepix detectors in the same positions as for alignment and αRAD measurements, with the PMMA phantom of different thicknesses and known WET. The energy deposition on detector # 5 was measured and with that data calibration curves were made (figure 27). Using the calibration curves, suitable energy was chosen for each region according to its predicted WET value from X-ray CT data. If the WET of the region has a value on the steep part of the calibration curve, that energy was chosen for irradiating the region. The steep part on the calibration curve shows large difference in WET for little change of energy deposition, which produce better αRAD image contrast.
If the predicted WET map (DRR) and the measured WET map directly be-

fore the patient treatment starts show a difference above a certain threshold, it means that the planning X-ray CT does not reflect the actual treatment situation.

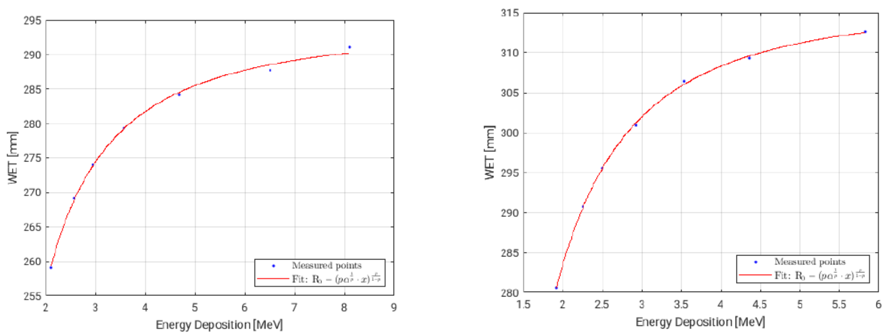

(a) 229.1 MeV/u

(b) 239.5 MeV/u

Figure 27: Calibration curves that provide a conversion of the energy deposition into the WET for each pixel. Reprinted from [45].

3.5 Data processing

This section describes the processing and analyzing of the measured data. The aim of the data processing is to remove background caused by detector artifacts and by secondary hydrogen ions that are mainly created by nuclear interactions of the primary helium ions with the atomic nuclei of the phantom. It is also used to match events through all detectors caused by the same helium ion and for a correct alignment of the six detectors. Data processing allows image reconstruction based on ion tracking and energy deposition (Cubic Spline Path (CSP) and Along Path Reconstruction (APR)). C++ and Matlab routines developed in the group have been used for these purposes.

3.5.1 Cluster classification

Raw data have been collected from each measurement. Six detectors record data files in frames in the form of clusters. After measurement, raw measured data have been processed and only "clean" data (clusters that have not been rejected by the classification) have been used for image reconstruction. The processing steps are explained in this section, while their results are presented in section 4.2.
Each time an ionizing radiation reaches the detector's sensitive surface, it produces a certain amount of charge depending on the type and energy of the radiation. The charge can spread because of Coulomb repulsion force and diffusion, also reaching neighboring pixels of the initially hit pixel. This effect

is called charge sharing and it is a factor limiting the energy resolution of the detector. Spreading of the charge causes collection by several adjacent pixels, generating a **cluster**. The most important cluster properties are listed in the table 1.

Property	Definition
Size	Number of pixel composing the cluster
Volume	Sum of pixel values (converted to energy)
Height	Maximum pixel value in the cluster

Table 1: Summary of cluster properties and their definitions.

Clusters acquired in energy mode have a 2D Gaussian profile, while clusters acquired in time mode show a nearly homogeneous signal. Not all detected clusters come from helium ions crossing the detector, some of them are secondary fragments or detector artifacts and they have to be removed (figure 28). Based on the operating mode of the detector, two types of cluster classifications have been applied.

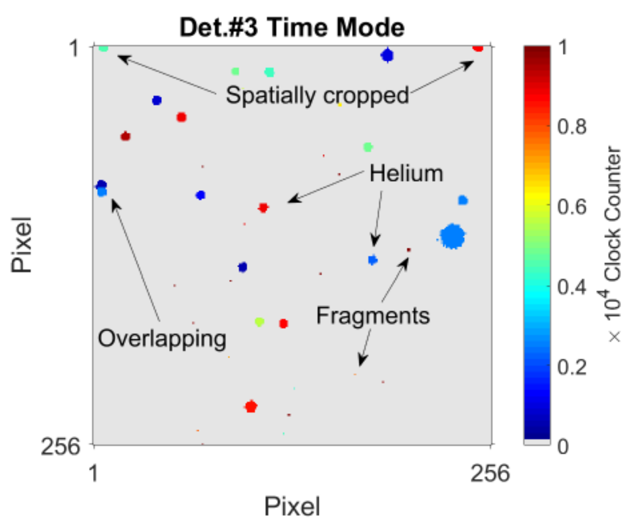

Figure 28: Example of a frame with clusters on detector in the time mode. Reprinted from [29].

Oscillations of the pixel electronics can cause a signal rise above the threshold. As a result, the pixel value is not only composed of the signal correlated to collected charge, but additionally to fake signal. This, is called **overshoot effect**. Clusters for which only the overshoot contributes to the signal are smaller than real clusters, so they can be easily excluded by the cluster size [40]. Figure

29 illustrates this effect. The clusters, arriving on the detector before a frame has started have a degraded cluster volume. One part of these clusters have a smaller cluster size therefore, they can be also excluded by the cluster size.

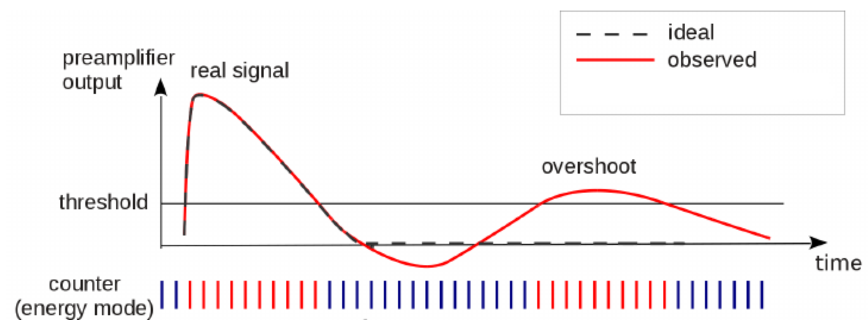

Figure 29: Illustration of the overshoot effect Reprinted from [40]

Short acquisition time disables the real signal and the overshoot effect to be included in the same frame. For this reason acquisition time $\leq 1\ ms$ would be desirable. On the other hand, the shorter the acquisition time is, the more clusters within the frame can not be completely digitized. This determines the lower limit of the acquisition time. In this work the acquisition time of $1\ ms$ was used as a compromise between these two competing criteria.
When two or more particles arrive to the detector close to each other, they create **overlapping clusters** (figure 28). Overlaps can be detected by analyzing the number of local maxima per cluster. Local maximum is defined as a pixel value, equal or bigger than all adjacent pixels and higher than 20% of the absolute maximum [46]. If two or more maxima were found in a cluster, that cluster was rejected.

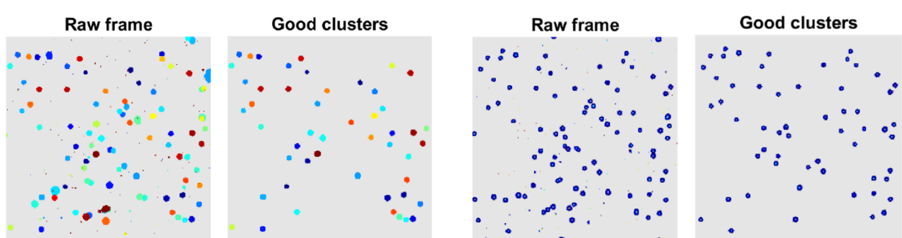

(a) (b)

Figure 30: Example of frame with raw data and frame after the cluster classification in (a) time mode and (b) energy mode. Reprinted from [29].

3.5.2 Particle tracking

The front and rear tracking systems determine the trace data of the single ions upstream and downstream of the phantom. Matched clusters through all the six detectors caused by the same helium ion are considered as one **matched event**. The matching process is illustrated in figure 31 and is based on the search for coincident hits on the Time detectors. This process is called *time matching*. The time of arrival at detectors operating in Time mode is used to determine the path of single ions. A coincidence window of ± 0.2 μm was applied for cluster pairs on the first two detectors, the second two detectors and also between the first two and the second two detectors. Time matching cannot be preformed in case of detector operating in Energy mode (detector #5), therefore the matching of clusters between detectors #5 and #6 is based on spatial information (*spatial matching*). The distances between the cluster at detector #6 and all the clusters at detector #5 are evaluated for each time-wise matched event. If the distance is less than 20 pixels (1.1 mm), clusters are matched, otherwise the event is dismissed. The spatial matching between detector #5 and detector #6 is only feasible for small incident angles (which is the case for the helium-beam radiography).

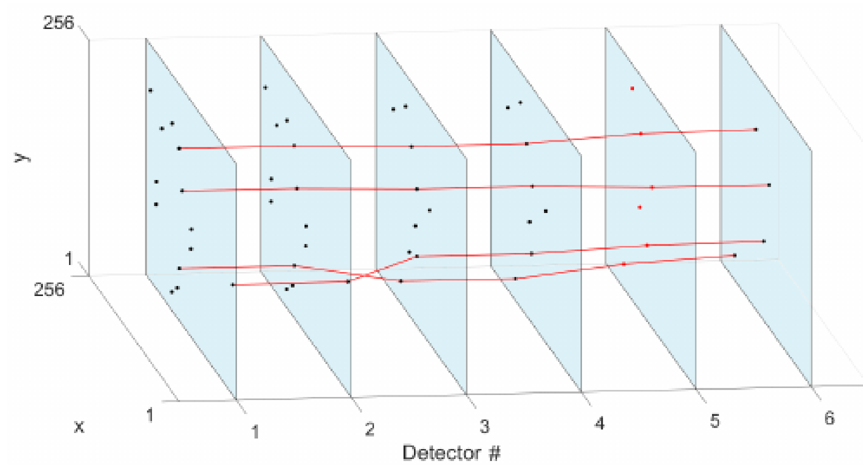

Figure 31: Schematic illustration of the matching algorithm. Reprinted from [29].

3.5.3 Image reconstruction

After filtering of the clusters with degraded information and matching procedure, a final step for the image formation was performed. To generate a radiography, it is important to have en estimation of the ion's path inside the phantom. The positions of the clusters at detectors # 1, # 2 and # 3,# 4 were used to reconstruct the paths of ions upstream and downstream of the phantom. With the known distances from phantom to the detectors and the assumption that ions have a linear path in the air, it is possible to determine the projection/backprojection of the ion track onto the front/back surface of the phantom. $r_o, \hat{d_o}$ and $r_1, \hat{d_1}$ are the position vectors and direction unit vectors at the front and back surface of the phantom [46]. For the estimation of the most likely path of the ion inside the phantom two algorithms were used.

- The first algorithm is called *Cubic Spline Path* (CSP) and it is a third degree polynomial function. The path inside the phantom was determined according to the following equation:

$$r(t) = (2t^3-3t^2+1)r_0+(t^3-2t^2+t)\Lambda_o^{opt}d_o+(-2t^3+3t^2)r_1+(t^3-t^2)\Lambda_1^{opt}d_1 \tag{12}$$

  where t is temporal parameter ranging between 0 and 1, $d_{o,1} = \hat{d}_{o,1}|r_1-r_0|$ and $\Lambda_{0,1}^{opt}$ is a scaling factor for the length of the direction vectors.

- For the second algorithm, called *Along Path Reconstruction* (APR), CSP was again used for the path estimation inside the phantom. The path was divided in 64 pixels along x and y, and 50 planes along z. The energy deposition of the ion in the detector (Δ E) was uniformly distributed along the particle's path (z axis). This procedure was repeated for each ion. The mean values of the energy deposition in each volume element (voxel) were then integrated along the z axis, obtaining 64 px x 64 px image.

4 Results and discussion

This chapter presents the results of the He-beam radiography of anthropomorphic pelvis phantom. Also, it describes the data processing and image reconstruction from processed data.

4.1 Experiments

All the experiments have been performed in the experimental room at The Heidelberg Ion-Beam Therapy Center (HIT, described in section 3.1). Settings of the beam used for the alignment and αRAD measurements are listed in the table 2 and detectors' settings are presented in table 3.

Ion	Helium	
Energy	229.1 MeV/u	239.5 MeV/u
Range	329.3 mm	354.8 mm
Intensity	$\approx$ 4.4 x 10^4 particles	
Modality	continuous shoots of 12 s + 5 s of dead time	

Table 2: Characteristics of the He-ion beam used for the experiments.

Detector	#1	#2	#3	#4	#5	#6
Position [mm]	0	3.65	439.5	443.5	465.0	469.0
Operating mode	Time of arrival				Energy mode	Time of arrival
Bias voltage	10 V					
Acquisition time	1 ms					

Table 3: Settings of the Timepix detectors used for the experiments.

First, the alignment measurements (described in section 3.3.1) were performed in order to precisely align all the detectors on the beam axis. The alignment measurements were carried out with six Timepix detectors and with no phantom and no BUM between them (figure 24).
Irradiation for the alignment measurements lasted 10 min for each of two He ion beam energies (229.1 MeV/u and 239.5 Mev/u). After merging the clusters from all six detectors over 2.6 x 10^6 clusters were stored in the processed file for each energy. Results of the alignment measurements for two energies are presented in table 4.
For the αRAD measurements the region of interest was divided in nine squares. For each of them the mean WET value was estimated from DRR based on X-ray CT. A rough WET value of each region was used in order to choose the adequate energy for each region. If WET is known, using the calibration curves presented in section 3.4, it is easy to choose the right energy. If the WET has a value on the

Coorection in direction [mm]	#1	#2	#3	#4	#5	#6	Energy
x	-8.421	-9.473	0	-0.098	-0.314	-0.378	229.1
y	1.223	0.056	0	-2.149	5.829	6.731	
x	-8.470	-9.499	0	-0.099	-0.321	-0.378	239.5
y	1.546	0.576	0	-2.145	5.832	6.711	

Table 4: Results of the alignment measurements for six detectors with isocenter on detector #3.

steep part of the calibration curve, the energy has been selected to irradiate the area. The steep part on the calibration curve shows large difference in WET for little change of energy deposition. Nine regions with the corresponding values are presented in table 5.

4.2 Data processing

This paragraph presents the results of data processing, which are described in section 3.5.

4.2.1 Cluster classification

A heatmap of all clusters (figure 32) and the remaining clusters (figure 33) shows the efficiency of data processing described in section 3.5.1. This heat map was obtained during energy deposition measurements of helium ions with $E = 239.6$ MeV/u. On the horizontal axes the clusters are sorted by size and volume, while the vertical axis shows relative number of clusters. The marked region by orange circle on figure 32, originates from secondary hydrogen ions and overshoot clusters (described in section 3.5.1), while the green circle presents ions with high energy deposition. Clusters with high energy deposition stop in detector # 5 and do not reach detector# 6, therefore they can not be matched and they are removed. The red opaque peak on figure 33 presents primary helium ions which are preserved after the selection procedures. Transparent regions indicate neglected clusters.
The contribution of secondary hydrogen ion clusters is around 10 %, while the contribution of clusters with high energy deposition is much smaller at around 0.2 %.

region 3 width: 300.78 mm WET: 303.19 mm energy: 239.5 MeV/u	region 2 width: 295.90 mm WET: 305.61 mm energy: 239.5 MeV/u	region 1 width: 290.03 mm WET: 294.97 mm energy: 229.1 Mev/u
region 4 width: 287.11 mm WET: 302.26 mm energy: 239.5 MeV/u	region 5 width: 290.04 mm WET: 300.37 mm energy: 239.5 MeV/u	region 6 width: 295.90 mm WET: 304.32 mm energy: 239.5 MeV/u
region 9 width: 272.46 mm WET: 289.51 mm energy: 229.1 Mev/u	region 8 width: 277.34 mm WET: 291.20 mm energy: 229.1 Mev/u	regin 7 width:282.23 mm WET: 295.69 mm energy: 229.1 MeV/u

Table 5: Arrangement of nine regions with the with width, WET and energy values for each of them.

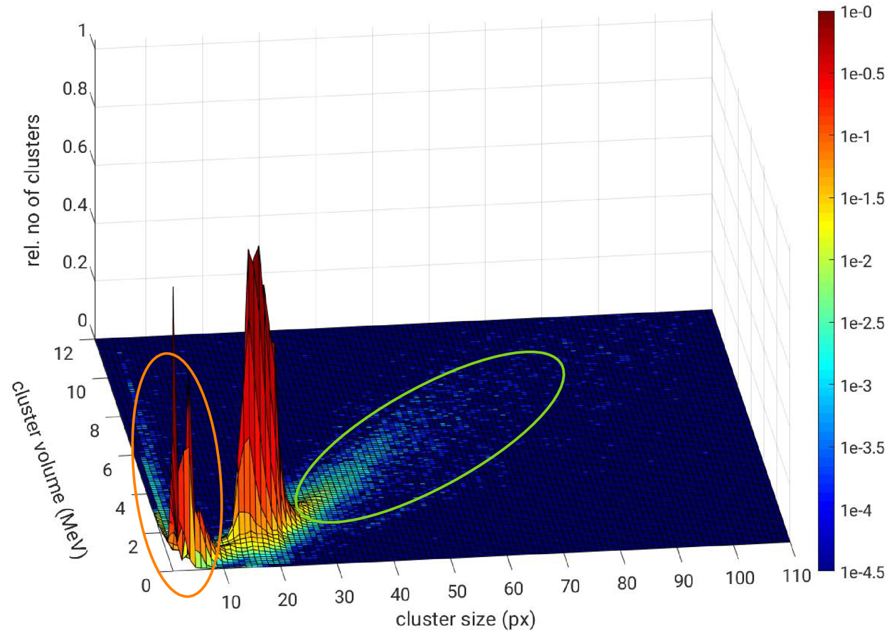

Figure 32: Heatmap of all clusters before the cluster classification.

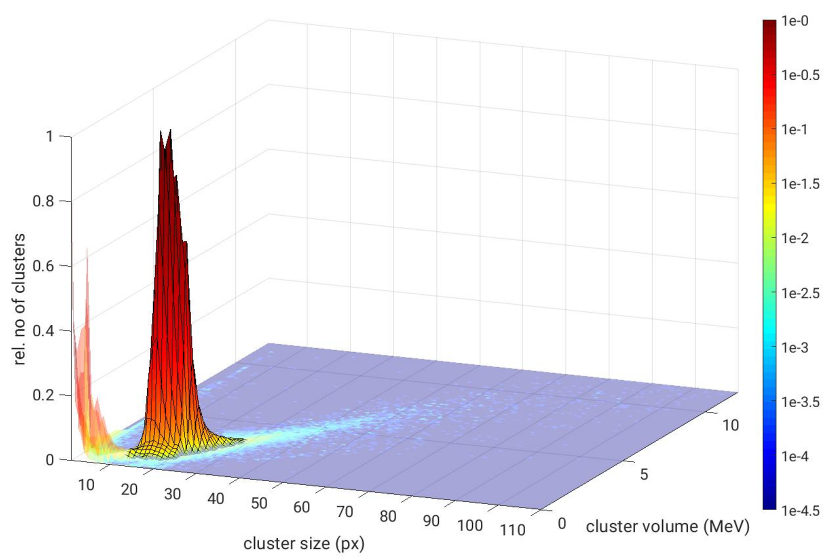

Figure 33: Heatmap of remaining clusters after the cluster classification.

4.2.2 Particle tracking

To reconstruct the path of each particle, it is important to match the clusters on the different detectors. The matching of signals performed between detectors operating in the time mode (#1, #2, #3, #4, #6) was performed using a coincidence window of 200 ns. The matching between signals on detector # 5 operating in energy mode and detector # 6 was performed using a spatial window of 1.1 mm. This process is described in section 3.5.2. The result of matching algorithm are matched events, which have been used to reconstruct the radiographs.
The matching efficiency is defined as a ratio of the total number of matched events on all six detectors (*Nmatch*) and good clusters on detector #6 (*Ndet.6*) [29]:

$$\eta^M = \frac{Nmatch}{Ndet.6} \tag{13}$$

Rejection of the clusters on detectors #1 to #5 during the cluster classification cause a decrease of matching efficiency. With too high beam intensity or big clusters, matching efficiency is lower because the probability of overlapping cluster increases. A matching efficiency of 100% would mean that all the good clusters on detector # 6 have been successfully matched.
The transmission efficiency is defined as a ratio of the number of primary ions that crossed all the detectors (good clusters on detector #6. *Ndet.6*) and the number of incoming helium ions (good clusters on detector #1, *Ndet.1*) [29]:

$$\eta^T = \frac{Ndet.6}{Ndet.1} \tag{14}$$

For each region the matching and the transmission efficiency are listed in the table 6. Figure 34 shows this two values during the measurement for one region.

Efficiency	Matching [%]	Transmission [%]
Region 1	28.05	38.27
Region 2	33.31	34.47
Region 3	35.42	35.63
Region 4	31.94	34.95
Region 5	32.85	34.88
Region 6	35.69	36.15
Region 7	34.63	29.87
Region 8	31.34	31.06
Region 9	29.83	31.46

Table 6: Matching and transmission efficiency for nine regions.

Matching and transmission efficiency values are important in order to evaluate

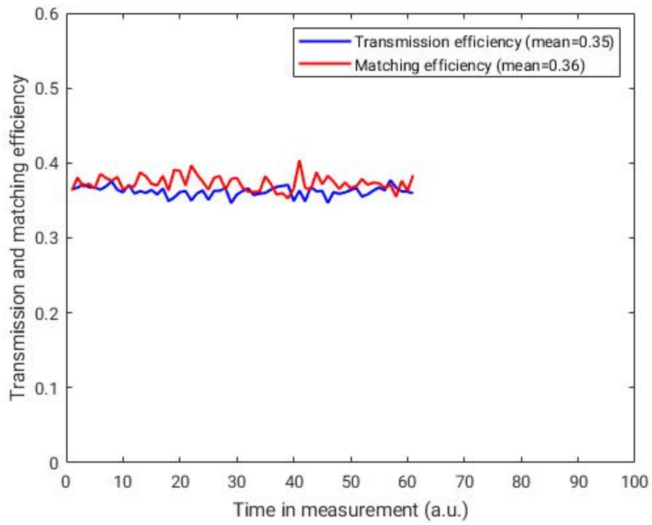

Figure 34: Transmission and matching efficiency of region 3 over the time of measurement.

the imaging dose in the end. The apsorbed dose is:

$$D = \frac{1 \cdot 10^5}{\eta^M \cdot \eta^T} \cdot D_{ion}, \tag{15}$$

where D_ion is the dose per primary helium ion. The η^M and η^T are estimated through experiment, while the D_{ion} is estimated through Monte Carlo simulations [29].

4.2.3 Image reconstruction

The result of this thesis is a helium-beam radiography of a region of interest within an anthropomorphic phantom of the region of interest composed of nine images. This radiography is also compared with a digitally reconstructed radiography (DRR) based on X-ray CT of the same region.
Figures 36a and 37a present the radiograph with clusters only originating from helium ions after data processing. Images have been reconstructed using two algorithms - Along Path Reconstruction (APR) and Cubic Spline Path (CSP), described in section 3.5.3. To compare images qualitatively two quantities described in section 2.4 have been used. The results show that the image reconstructed using APR algorithm (figure 36a) has better contrast to noise ratio than image reconstructed using CSP algorithm (figure 37a). On the other hand, image reconstructed using CSP algorithm has better spatial resolution.

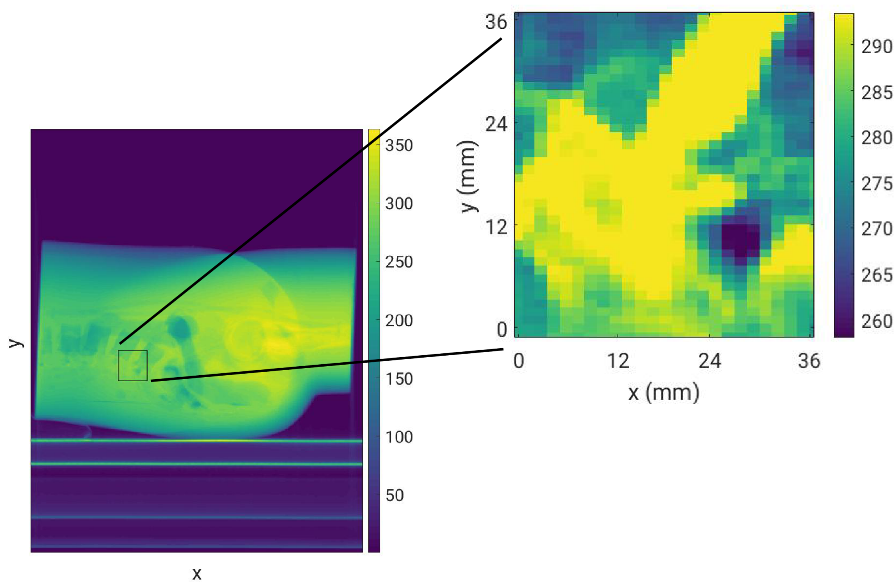

Figure 35: Digitally reconstructed radiography (DRR) of the phantom based on X-ray CT. A marked square region shows the region of interest (36 x 36 mm) for performed αRAD . Colourbars on the right side on both images show reconstructed WET values in mm.

The final αRAD images were found to be in agreement with DRR, but comparison has to be finalized in a further study. Potential differences between them could be related to the known uncertainties of X-ray CT data, but also to remaining problems in calibration process (dE/dx to WET) which has to be solved.
In the final αRAD images (figure 36a and 37a) right upper corner (region 1)

shows poor resolution caused probably by wrong choice of the beam energy. Left side of this region is really dense due to the presence of bone, hence ions were stopped before reaching the energy detector behind the phantom.

Also, there is an issue of WET determination between the images with the energy of 239.5 MeV and 229.1 MeV. So, the first attempt to implement the calibration procedure for a radiograph of an anthropomorphic phantom did not completely work. This means that transition issues between the images of different energy have to be further investigated and the calibration curve of each energy has to be verified in another measurement.

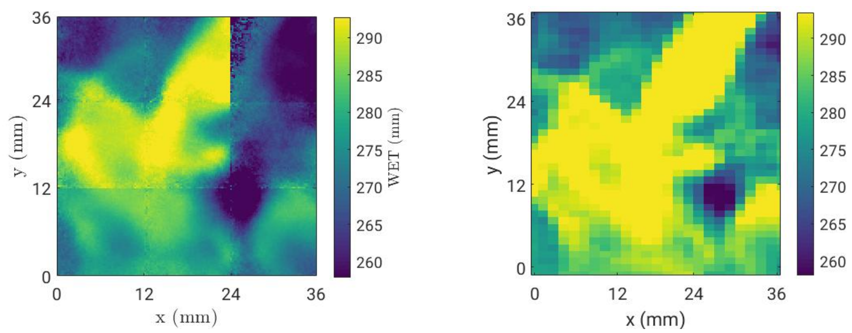

(a) (b)

Figure 36: Comparation of αRAD image reconstructed using APR algorithm (a), and DRR (b).

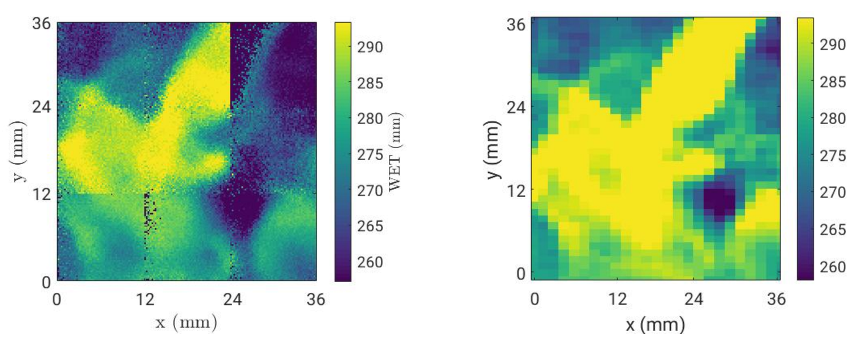

(a) (b)

Figure 37: Comparation of αRAD image reconstructed using CSP algorithm (a), and DRR (b).

5 Conclusion

The long-term motivation of this thesis was to improve ion-beam radiotherapy treatments with performing ion-beam radiography (iRAD) in addition to the imaging techniques that are used for treatment planning nowadays. Currently, the most important imaging technique for treatment planning of ion-beam therapy is X-ray CT. However, the conversion of the attenuation of X-rays into ion stopping power produce uncertainties of the ion range of about 3%. iRAD has a potential benefit since the imaging and treatment radiation are identical which avoid conversion errors. iRAD enables the direct measurement of the integrated relative stopping power of the ions crossing the patient, and the method can be used with the patient being already in treatment position. With this information the correct positioning of the patient could be performed and it could be verified that appropriate energies were chosen in order to adjust the Bragg peak to the depth of the tumor.

In the present thesis a method of helium-beam radiography (αRAD) has been investigated. The technique for αRAD , based on single-ion tracking system has been developed at the German Cancer Research Center (DKFZ) in Heidelberg, Germany.

The detection system is composed of pixelated detectors, Timepix, developed at CERN in the Medipix Collaboration. Six parallel Timepix detectors have been used for front and rear tracking systems, and for an energy detection system. The tracking systems, positioned upstream and downstream of the phantom, have been used to measure position and direction of incoming and outgoing ions. The energy detection system has been used for energy deposition measurements with additional time information. Measuring the energy loss of the ions in the detector provides the image contrast. The steep rising part of the Bragg peak has been placed at the energy detector. With this, it was possible to measure large changes in energy deposition for small changes in the WET of the phantom, enabligh high-contrast imaging.

Nuclear fragmentation of helium ions cause the production of secondary hydrogen ions. They also reach the energy detector and lead to a noisy images. Because of that, it is important to distinguish secondary fragments from primary helium ions during the imaging process. The presented detection system can identify the ion type, which enables the elimination of the secondary hydrogen ions in post-processing phase. Also, in the data processing, it is possible to remove fake signals on the detectors caused by detector artifacts.

All these processes were modified and further developed for the application on an anthropomorphic pelvis phantom. A new set of helium-beam energies that are higher than energies relevant for radiation treatment with preliminary accelerator settings (229.1 MeV/u and 239.5 MeV/u) at the Heidelberg Ion-Beam Therapy Center (HIT) could be used for the first time, enabling αRAD of a thick anthropomorphic phantom. WETs measured by αRAD have the same validity as WETs measured by proton and carbon beams. Helium-beams have been chosen because it suffers less multiple Coulomb scattering than proton-beams and less fragmentation than carbon-beams. In the end the WET map of the

region of interest obtained from the αRAD have been compared qualitatively with the WET map acquired from digitally reconstructed radiography (DRR) based on the planning X-ray CT.
To summarize, the presented study has shown the advantage of αRAD and its first application on an anthropomorphic pelvis phantom. αRAD might upgrade ion-beam radiotherapy treatments, but for a potential clinical application further improvements of this method are required.

Bibliography

References

[1] Max LM Boone, John H Lawrence, William G Connor, Richard Morgado, John A Hicks, and Richard C Brown. Introduction to the use of protons and heavy ions in radiation therapy: historical perspective. *International Journal of Radiation Oncology* Biology* Physics*, 3:65–69, 1977.

[2] Tim Gehrke. *Helium-beam Radiography with a Fully Pixelated Silicon Detection System.* PhD thesis, Ruperto-Carola University of Heidelberg, 2018.

[3] M Jermann. Particle therapy patient statistics (per end of 2018).

[4] William Henry Bragg and RLXXIV Kleeman. Lxxiv. on the ionization curves of radium. *The London, Edinburgh, and Dublin Philosophical Magazine and Journal of Science*, 8(48):726–738, 1904.

[5] Allan Macleod Cormack. Representation of a function by its line integrals, with some radiological applications. *Journal of applied physics*, 34(9):2722–2727, 1963.

[6] Gavin Poludniowski, NM Allinson, and PM Evans. Proton radiography and tomography with application to proton therapy. *The British journal of radiology*, 88(1053):20150134, 2015.

[7] Uwe Schneider and Eros Pedroni. Proton radiography as a tool for quality control in proton therapy. *Medical physics*, 22(4):353–363, 1995.

[8] PJ Doolan, M Testa, G Sharp, EH Bentefour, G Royle, and HM Lu. Patient-specific stopping power calibration for proton therapy planning based on single-detector proton radiography. *Physics in Medicine & Biology*, 60(5):1901, 2015.

[9] Dieter Schardt, Thilo Elsässer, and Daniela Schulz-Ertner. Heavy-ion tumor therapy: Physical and radiobiological benefits. *Reviews of modern physics*, 82(1):383, 2010.

[10] Ute Linz. *Ion beam therapy: fundamentals, technology, clinical applications.* Springer Science & Business Media, 2011.

[11] L Opalka, C Granja, B Hartmann, J Jakubek, O Jaekel, M Martisikova, S Pospisil, and J Solc. 3d measurement of the radiation distribution in a water phantom in a hadron therapy beam. *Journal of Instrumentation*, 7(01):C01085, 2012.

[12] T Gehrke, C Amato, S Berke, and M Martišíková. Theoretical and experimental comparison of proton and helium-beam radiography using silicon pixel detectors. *Physics in Medicine & Biology*, 63(3):035037, 2018.

[13] Wayne D Newhauser and Rui Zhang. The physics of proton therapy. *Physics in Medicine & Biology*, 60(8):R155, 2015.

[14] Bernard Gottschalk. Physics of proton interactions in matter. *Proton therapy physics. USA: Taylor & Francis Inc*, pages 20–57, 2012.

[15] William R Leo. *Techniques for nuclear and particle physics experiments: a how-to approach*. Springer Science & Business Media, 2012.

[16] Peter Sigmund, R Bimbot, H Geissel, H Paul, and A Schinner. Stopping of ions heavier than helium. 2005.

[17] Devesh Kumar Avasthi and Girijesh Kumar Mehta. *Swift heavy ions for materials engineering and nanostructuring*, volume 145. Springer Science & Business Media, 2011.

[18] DC Williams. The most likely path of an energetic charged particle through a uniform medium. *Physics in Medicine & Biology*, 49(13):2899, 2004.

[19] K Gunzert-Marx, H Iwase, D Schardt, and RS Simon. Secondary beam fragments produced by 200 mev u- 1 12c ions in water and their dose contributions in carbon ion radiotherapy. *New journal of physics*, 10(7):075003, 2008.

[20] Solange Gagnebin, Damian Twerenbold, Eros Pedroni, David Meer, Silvan Zenklusen, and Christian Bula. Experimental determination of the absorbed dose to water in a scanned proton beam using a water calorimeter and an ionization chamber. *Nuclear Instruments and Methods in Physics Research Section B: Beam Interactions with Materials and Atoms*, 268(5):524–528, 2010.

[21] Rebecca Antonia Grün. Impact of tissue specific parameters on the predition of the biological effectiveness for treatment planning in ion beam therapy. 2014.

[22] James D Cox and Kie Kian Ang. *Radiation Oncology E-Book: Rationale, Technique, Results.* Elsevier Health Sciences, 2009.

[23] Seo Hyun Park and Jin Oh Kang. Basics of particle therapy i: physics. *Radiation oncology journal*, 29(3):135, 2011.

[24] Olga Sokol. *Oxygen ions as a single and combined modality in radiotherapy.* PhD thesis, Technische Universität, 2018.

[25] International Commission on Radiation Units. *Quantities and units in radiation protection dosimetry.* Intl Commission on Radiation, 1993.

[26] William T Chu. Overview of light-ion beam therapy. 2006.

[27] Rui Zhang, Phillip J Taddei, Markus M Fitzek, and Wayne D Newhauser. Water equivalent thickness values of materials used in beams of protons, helium, carbon and iron ions. *Physics in Medicine & Biology*, 55(9):2481, 2010.

[28] Helmuth Spieler. *Semiconductor detector systems*, volume 12. Oxford university press, 2005.

[29] Carlo Amato. Helium-beam radiography and spatial resolution improvement. 2017.

[30] Th Haberer, Jürgen Debus, H Eickhoff, Oliver Jäkel, Daniela Schulz-Ertner, and Uli Weber. The heidelberg ion therapy center. *Radiotherapy and Oncology*, 73:S186–S190, 2004.

[31] D Ondreka and U Weinrich. The heidelberg ion therapy (hit) accelerator coming into operation. In *Proc. 11th European Particle Accelerator Conference (EPAC'08)*, pages 979–981, 2008.

[32] A Dolinskii, H Eickhoff, and B Franczak. The synchrotron of the dedicated ion beam facility for cancer therapy, proposed for the clinic in heidelberg'. In *EPAC'00, Vienna*, page 2509, 2000.

[33] M Krämer, O Jäkel, T Haberer, E Rietzel, D Schardt, M Scholz, JF Wang, U Weber, and W Weyrather. Treatment planning for scanned ion beams. *Radiotherapy and Oncology*, 73:S80–S85, 2004.

[34] Christian Schömers, Eike Feldmeier, Michael Galonska, Stefan Scheloske, Andreas Peters, Thomas Haberer, and Rainer Cee. Reacceleration of ion beams for particle therapy. 2014.

[35] Katia Parodi, Andrea Mairani, Stephan Brons, Bernd-Georg Hasch, Florian Sommerer, Jakob Naumann, Oliver Jäkel, Thomas Haberer, and Jürgen Debus. Monte carlo simulations to support start-up and treatment planning of scanned proton and carbon ion therapy at a synchrotron-based facility. *Physics in Medicine & Biology*, 57(12):3759, 2012.

[36] Xavier Llopart, Rafael Ballabriga, Michael Campbell, Lukas Tlustos, and Winnie Wong. Timepix, a 65k programmable pixel readout chip for arrival time, energy and/or photon counting measurements. *Nuclear Instruments and Methods in Physics Research Section A: Accelerators, Spectrometers, Detectors and Associated Equipment*, 581(1-2):485–494, 2007.

[37] M Martišíková, T Gehrke, S Berke, G Aricò, and O Jäkel. Helium ion beam imaging for image guided ion radiotherapy. *Radiation oncology*, 13(1):109, 2018.

[38] ADVACAM s.r.o. Timepix detector. http://www.widepix.cz/index.php?p=products, accessed December 12, 2019.

[39] V Kraus, Michael Holik, Jan Jakubek, M Kroupa, P Soukup, and Z Vykydal. Fitpix—fast interface for timepix pixel detectors. *Journal of Instrumentation*, 6(01):C01079, 2011.

[40] Bernadette Hartmann. *A novel approach to ion spectroscopy of therapeutic ion beams using a pixelated semiconductor detector*. PhD thesis, 2013.

[41] Jan Jakubek. Energy-sensitive x-ray radiography and charge sharing effect in pixelated detector. *Nuclear Instruments and Methods in Physics Research Section A: Accelerators, Spectrometers, Detectors and Associated Equipment*, 607(1):192–195, 2009.

[42] RPM Van der Boog. Energy calibration procedure of a pixel detector. *Bachelor thesis of applied physics (B. Eng.), The Hague university of applied sciences*, 2013.

[43] Jan Jakubek. Precise energy calibration of pixel detector working in time-over-threshold mode. *Nuclear Instruments and Methods in Physics Research Section A: Accelerators, Spectrometers, Detectors and Associated Equipment*, 633:S262–S266, 2011.

[44] Bo Shi et al. *Coherent X-ray scattering of charge order dynamics and phase separation in titanates*. PhD thesis, Universiteit van Amsterdam, 2017.

[45] Catherine Knobloch. Wet calibration for helium beam radiography, bachelor thesis. 2020.

[46] Tim Gehrke, L Burigo, Giulia Arico, S Berke, J Jakubek, D Turecek, T Tessonnier, A Mairani, and M Martišíková. Energy deposition measurements of single 1h, 4he and 12c ions of therapeutic energies in a silicon pixel detector. *Journal of Instrumentation*, 12(04):P04025, 2017.

Biografija

Sonja Surla rođena je 08.04.1994. godine u Novom Sadu. Završila je osnovnu školu „Prva Vojvođanska brigada“ sa Vukovom diplomom i gimnaziju „Isidora Sekulić“ u Novom Sadu. 2018. godine završila je osnovne akademske studije fizike sa stručnim nazivom - Diplomirani profesor fizike, na Prirodno-Matematičkom fakultetu u Novom Sadu. Iste godine je upisala i master studije na Katedri za nuklearnu fiziku. Dobitnik je stipendije Ministarstva prosvete i ERASMUS projekta. Deo master studija je provela u Hajdelbergu u Nemačkoj kao učesnik programa razmene studenata. U Nemačkom centru za istraživanje raka (Deutsches Krebsforschungszentrum) u Hajdelbergu je pisala master rad. Eksperimentalni deo master rada je radila u Centru za terapiju ubrzanim jonima (Heidelberger Ionenstrahl-Therapiezentrum, HIT).

UNIVERZITET U NOVOM SADU
PRIRODNO-MATEMATIČKI FAKULTET

KLJUČNA DOKUMENTACIJSKA INFORMACIJA

Redni broj:	
RBR	
Identifikacioni broj:	
IBR	
Tip dokumentacije:	Monografska dokumentacija
TD	
Tip zapisa:	Tekstualni štampani materijal
TZ	
Vrsta rada:	Master rad
VR	
Autor:	Sonja Surla
AU	
Mentor:	Prof. dr Jovana Nikolov, vanredni profesor
MN	
Naslov rada:	Kvantitativna radiografija helijumskim snopom sa primenom na antropomorfni karlični fantom
NR	
Jezik publikacije:	engleski
JP	
Jezik izvoda:	srpski
JI	
Zemlja publikovanja:	Srbija
ZP	
Uže geografsko područje:	Vojvodina
UGP	
Godina:	2020
GO	

Izdavač:	Autorski reprint
IZ	
Mesto i adresa:	Prirodno-matematički fakultet, Trg Dositeja Obradovića 4, Novi Sad
MA	
Fizički opis rada:	5 poglavlja/45 strana/46 referenci/37 slika/6 tabeli
FO	
Naučna oblast:	Fizika
NO	
Naučna disciplina:	Nuklearna fizika
ND	
Predmetna odrednica/ ključne reči:	Radioterapija, radiografija, ubrzani joni helijuma,
PO	
UDK	
Čuva se:	Biblioteka departmana za fiziku, PMF-a u Novom Sadu
ČU	
Važna napomena:	nema
VN	
Izvod: **IZ**	U radu su prikazani rezultati radiografije ubrzanim jonima, prvi put primenjene na antropomorfni karlični fantom. Cilj radiografije ubrzanim jonima je preciznije pozicioniranje ubrzanih jona za radioterapiju u okviru tumora.
Datum prihvatanja teme od NN veća: **DP**	06.01.2020.
Datum odbrane: **DO**	10.01.2020.
Članovi komisije:	
KO	
Predsednik:	Prof dr Jovana Nikolov, vanredni profesor, PMF u Novom Sadu
član:	Prof. dr Dušan Mrđa, redovni profesor, PMF u Novom Sadu
član:	Prof. dr Maja Stojanović, redovni profesor, PMF u Novom Sadu

UNIVERSITY OF NOVI SAD

FACULTY OF SCIENCE AND MATHEMATICS

KEY WORDS DOCUMENTATION

Accession number: **ANO**	
Identification number: **INO**	
Document type: **DT**	Monograph publication
Type of record: **TR**	Textual printed material
Content code: **CC**	Final paper
Author: **AU**	Sonja Surla
Mentor/comentor: **MN**	Prof. dr Jovana Nikolov, associate professor, Faculty of Sciences, Novi Sad
Title: **TI**	Quantitative helium-beam radiography of an anthropomorphic pelvis phantom
Language of text: **LT**	English
Language of abstract: **LA**	English
Country of publication: **CP**	Serbia
Locality of publication: **LP**	Vojvodina

Publication year: **PY**	2020
Publisher: **PU**	Author's reprint
Publication place: **PP**	Faculty of Science and Mathematics, Trg Dositeja Obradovića 4, Novi Sad
Physical description: PD	5/182/32/0/71/0/3
Scientific field: **SF**	Physics
Scientific discipline: **SD**	Nuclear Physics
Subject/ Key words: **SKW**	Ion-beam Radiotherapy, Ion-beam Radiography, Helium-ion beam
UC	
Holding data: **HD**	Library of Department of Physics, Trg Dositeja Obradovića 4
Note: **N**	none
Abstract: **AB**	The results of helium ion-beam radiography of an anthropomorphic pelvis phantom are presented in this thesis. The aim of ion-beam radiography is is the precise positioning of accelerated ions for radiotherapy inside the tumor.
Accepted by the Scientific Board: **ASB**	06.01.2020.
Defended on: **DE**	10.01.2020.
Thesis defend board: **DB**	
President:	Prof dr Jovana Nikolov, associate professor, Faculty of Sciences, Novi Sad

Member: Prof. dr Dušan Mrđa, full professor, Faculty of Sciences, Novi Sad

Member: Prof. dr Maja Stojanović, full professor, Faculty of Sciences, Novi Sad